Journal of Quantitative Spectroscopy & Radiative Transfer 137 (2014) 29–50

Contents lists available at ScienceDirect

Journal of Quantitative Spectroscopy & Radiative Transfer

journal homepage: www.elsevier.com/locate/jqsrt

GARLIC — A general purpose atmospheric radiative transfer line-by-line infrared-microwave code: Implementation and evaluation ☆

Franz Schreier [a,*], Sebastián Gimeno García [a], Pascal Hedelt [a], Michael Hess [a,b], Jana Mendrok [c], Mayte Vasquez [a], Jian Xu [a]

[a] DLR — German Aerospace Center, Remote Sensing Technology Institute, Oberpfaffenhofen, 82234 Weßling, Germany
[b] RASCIN, Thalkirchner Str. 284, 81371 München, Germany
[c] Division of Space Technology, Lulea University of Technology, Kiruna, Sweden

ARTICLE INFO

Article history:
Received 28 June 2013
Received in revised form
22 November 2013
Accepted 27 November 2013
Available online 5 December 2013

Keywords:
Radiative transfer
Infrared
Microwave
Molecular absorption
Line-by-line

ABSTRACT

A suite of programs for high resolution infrared-microwave atmospheric radiative transfer modeling has been developed with emphasis on efficient and reliable numerical algorithms and a modular approach appropriate for simulation and/or retrieval in a variety of applications. The Generic Atmospheric Radiation Line-by-line Infrared Code — GARLIC — is suitable for arbitrary observation geometry, instrumental field-of-view, and line shape. The core of GARLIC's subroutines constitutes the basis of forward models used to implement inversion codes to retrieve atmospheric state parameters from limb and nadir sounding instruments.

This paper briefly introduces the physical and mathematical basics of GARLIC and its descendants and continues with an in-depth presentation of various implementation aspects: An optimized Voigt function algorithm combined with a two-grid approach is used to accelerate the line-by-line modeling of molecular cross sections; various quadrature methods are implemented to evaluate the Schwarzschild and Beer integrals; and Jacobians, i.e. derivatives with respect to the unknowns of the atmospheric inverse problem, are implemented by means of automatic differentiation. For an assessment of GARLIC's performance, a comparison of the quadrature methods for solution of the path integral is provided. Verification and validation are demonstrated using intercomparisons with other line-by-line codes and comparisons of synthetic spectra with spectra observed on Earth and from Venus.

© 2013 The Authors. Published by Elsevier Ltd. All rights reserved.

1. Introduction

Radiative transfer [1–3] plays a central role in atmospheric science (e.g., remote sensing, meteorology, and climatology) and related branches of astronomy and astrophysics, and a large variety of codes have been developed differing in (level of) sophistication, spectral domain, and resolution. Thanks to increases in computational power, high resolution infrared (IR) and microwave (MW) radiative transfer calculations by means of "line-by-line" (lbl) models — once a challenge even for big machines — has become widely available.

Although lbl models are still computationally demanding, they are indispensable for the analysis of high resolution spectra delivered by a growing fleet of space-borne IR/MW sensors and some dozens of ground-based spectrometers (e.g., in the framework of NDACC, the Network for the Detection of Atmospheric Composition

☆ This is an open-access article distributed under the terms of the Creative Commons Attribution License, which permits unrestricted use, distribution, and reproduction in any medium, provided the original author and source are credited.

* Corresponding author. Tel.: +49 8153 28 1234; fax: +49 8153 28 1446.
E-mail address: franz.schreier@dlr.de (F. Schreier).

0022-4073/$ - see front matter © 2013 The Authors. Published by Elsevier Ltd. All rights reserved.
http://dx.doi.org/10.1016/j.jqsrt.2013.11.018

Change, http://www.ndacc.org) and several airborne or balloon-borne instruments (e.g., [4–8]). Furthermore, lbl models are mandatory to generate and verify fast parameterized radiative transfer models based on band model [9], k-distribution/correlated-k [10], exponential sum fitting [11] or emissivity-growth approximations [12] utilized for numerical weather forecasting and climate models. Finally, lbl models are required in the rapidly growing field of extrasolar planet remote sensing. Although band models etc., have been developed for other planets as well (e.g., [13–15]) and exoplanet spectra will likely be available only with limited resolution and considerable noise levels in the near future, the use of fast parameterized radiative transfer models typically developed for a limited range of atmospheric conditions (mostly Earth-like) can be dangerous and the greater flexibility of lbl models is advantageous to cope with these largely unknown atmospheric conditions.

Despite significant progress, lbl-modeling is still challenging in view of the rapidly growing number of Earth (and (exo-)planet) observation systems producing more and more data with increasing resolution and decreasing noise levels. For example, during its 10 years lifetime (2002–2012) MIPAS (Michelson Interferometer for Passive Atmospheric Sounding) observed about 80 million spectra [16], whereas the infrared limb imager of PREMIER (PRoCess Exploration through Measurements of Infrared and millimetre-wave Emitted Radiation [17]), a candidate for ESA's Earth Explorer 7 mission, would have delivered 12 000 limb images comprising 15 million radiance spectra per day. Furthermore, the amount and quality of spectroscopic line parameters is continuously increasing, from about 0.1 million in the first release (1972, then known as the AFGL tape) to about 7.5 million lines in the current 2012 edition of the HITRAN database [18], and many millions of lines in dedicated databases such as HITEMP [19] or ExoMol [20].

The lbl calculation of molecular absorption cross sections is generally the most time consuming part of a high resolution radiative transfer computation. The approach to tackle this challenge is probably the most distinct feature of the various codes developed, starting with the early works of, e.g., FASCODE and 4A [21,22]. Some widely used lbl codes developed later include GENLN2 [23], LBLRTM (based on FASCODE [24]), or ARTS [25,26].

When our code development started in the mid-90s, the number of publicly available lbl codes was quite limited, especially with retrieval applications in mind. Neither FASCODE nor GENLN2 provides analytical derivatives important for nonlinear optimization schemes, where the radiative transfer code serves as forward model. The option to evaluate analytical Jacobians has been implemented in 2004 in LBLRTM (v9.2). ARTS [25] evaluates molecular concentration derivatives analytically and uses a semi-analytic approach for some other variables. Job specification for FASCODE is cumbersome and error prone as dozens of variables have to be given in a strictly formatted input file (the so-called "`TAPE5`"). Furthermore, computation of a series of viewing geometries, e.g., for finite field-of-view and/or limb sequences, has to be performed manually with a series of jobs, so invariant quantities (e.g., molecular cross sections) have to be recalculated again and again. Finally note that FASCODE is closely linked to the HITRAN spectroscopic database [19], hence inclusion of molecules not covered by HITRAN is almost impossible.

In view of these shortcomings, development of a new code was started in the mid-90s (early versions of the code are described in conference proceedings [27,28]). Use of modern, efficient and accurate numerical algorithms has been an important design principle from the beginning, and verification and validation have been an integral and essential aspect of the code development that has been addressed in several ways. Apart from frequent comparisons with FASCODE, the new code has been participating in two extensive intercomparison studies assessing the performance of thermal infrared [29] and microwave [30] radiative transfer models.

This paper is organized in five sections: In the next section, we briefly review the physical basis of infrared and microwave radiative transfer with high spectral resolution, i.e. line-by-line modeling (for brevity "microwave" is not always mentioned in the following). In Section 3, we present GARLIC (Generic Atmospheric Radiation Line-by-line Infrared Code) providing an extensive discussion of numerical and computational approximations and implementation aspects. The performance is evaluated in Section 4, and a summary and outlook is given in Section 5.

2. Atmospheric radiative transfer and molecular absorption

2.1. Infrared and microwave radiative transfer

In a gaseous cloud and aerosol free atmosphere, scattering usually does not significantly contribute to IR extinction, and radiative transfer is described by the Schwarzschild equation [1–3]. For an arbitrary slant path, the intensity (radiance) I at wavenumber ν and position $s=0$ is given by the integral along the line-of-sight:

$$I(\nu) = I_\mathrm{b}(\nu)\exp\left(-\int_0^{s_\mathrm{b}} \alpha(\nu,s)\,\mathrm{d}s\right) + \int_0^{s_\mathrm{b}} J(\nu,s')\,\mathrm{e}^{-\int_0^{s'}\alpha(\nu,s'')\,\mathrm{d}s''}\alpha(\nu,s')\,\mathrm{d}s' \tag{1a}$$

$$I(\nu) = I_\mathrm{b}(\nu)\,\mathrm{e}^{-\tau_\mathrm{b}(\nu)} + \int_0^{\tau_\mathrm{b}} J(\nu,\tau')\,\mathrm{e}^{-\tau'}\,\mathrm{d}\tau' \tag{1b}$$

$$I(\nu) = I_\mathrm{b}(\nu)\mathcal{T}_\mathrm{b}(\nu) + \int_{\mathcal{T}_\mathrm{b}(\nu)}^{1} J(\nu,\mathcal{T})\,\mathrm{d}\mathcal{T} \tag{1c}$$

where the first term describes an attenuated background contribution I_b at position s_b. In case of a nadir viewing geometry, the background is the emission and reflection from the Earth's (or planet's) surface, whereas in case of an uplooking or limb-viewing geometry the integral practically terminates at the "top-of-atmosphere" (ToA). Furthermore, assuming local thermodynamical equilibrium, the source function J depends on temperature T

only and is given by the Planck function:

$$B(\nu,T)=\frac{2hc^2\nu^3}{\exp(hc\nu/k_\mathrm{B}T)-1}, \tag{2}$$

with c, h, and k_B denoting speed of light, Planck constant, and Boltzmann constant, respectively.

The optical depth τ, measured relative to the observer (at $s=\tau=0$), and the monochromatic transmission $\mathcal{T}$ are given according to Beer's law by

$$\mathcal{T}(\nu,s)=\mathrm{e}^{-\tau(\nu,s)}=\exp\left(-\int_0^s \alpha(\nu,s')\,\mathrm{d}s'\right)$$
$$=\exp\left(-\int_0^s \mathrm{d}s'\sum_m k_m(\nu,p(s'),T(s'))n_m(s')\right) \tag{3}$$

where p is the atmospheric pressure and α is the absorption coefficient, that is essentially determined by the sum of the absorption cross sections k_m scaled by the molecular number densities n_m.

Instrumental effects are modeled by convolution of the monochromatic intensity (1) or transmission (3) with appropriate spectral response functions (SRF, or instrument line shape, ILS) and field-of-view (FoV) functions.

2.2. Molecular absorption

In high resolution line-by-line models, the absorption cross section of molecule m (for brevity the subscript is omitted henceforth) is given by the superposition of many lines l with line center positions $\hat{\nu}_l$, each described by the product of a temperature-dependent line strength S_l and a normalized line shape function g describing the broadening mechanism(s):

$$k(\nu,p,T)=\sum_l S_l(T)\,g(\nu;\hat{\nu}_l,\gamma_l(p,T)). \tag{4}$$

For the infrared and microwave spectral regime, the combined effect of pressure broadening (with a half width essentially proportional to pressure, $\gamma_\mathrm{L}\propto p$) corresponding to a Lorentzian line shape:

$$g_\mathrm{L}(\nu-\hat{\nu},\gamma_\mathrm{L})=\frac{\gamma_\mathrm{L}/\pi}{(\nu-\hat{\nu})^2+\gamma_\mathrm{L}^2}, \tag{5}$$

and Doppler broadening, corresponding to a Gaussian line shape:

$$g_\mathrm{G}(\nu-\hat{\nu},\gamma_\mathrm{G})=\frac{\sqrt{\ln 2/\pi}}{\gamma_\mathrm{G}}\cdot\exp\left[-\ln 2\left(\frac{\nu-\hat{\nu}}{\gamma_\mathrm{G}}\right)^2\right] \tag{6}$$

with $\gamma_\mathrm{G}\propto\hat{\nu}\sqrt{T}$ can be represented by a Voigt line profile [31]:

$$g_\mathrm{V}(\nu-\hat{\nu},\gamma_\mathrm{L},\gamma_\mathrm{G})=g_\mathrm{L}\otimes g_\mathrm{G}$$
$$=\int_{-\infty}^{\infty}\mathrm{d}\nu' g_\mathrm{L}(\nu-\nu',\gamma_\mathrm{L})\times g_\mathrm{G}(\nu'-\hat{\nu},\gamma_\mathrm{G}) \tag{7}$$

In the microwave regime, a correction of the Lorentz profile is provided by the van Vleck–Weisskopf (or van Vleck–Huber) profile [1,23,25]:

$$g_\mathrm{VVW}(\nu,\hat{\nu},\gamma_\mathrm{L})=\left(\frac{\nu}{\hat{\nu}}\right)^2\left(\frac{\gamma_\mathrm{L}/\pi}{(\nu-\hat{\nu})^2+\gamma_\mathrm{L}^2}+\frac{\gamma_\mathrm{L}/\pi}{(\nu+\hat{\nu})^2+\gamma_\mathrm{L}^2}\right). \tag{8}$$

Pressure induced line shifts lead to $\hat{\nu}\longrightarrow\hat{\nu}+p\delta$ in Eqs. (5) and (7), where δ is the shift parameter as given by HITRAN [18] or GEISA [32,33].

The line-by-line cross sections according to Eqs. (4)–(8) do not completely describe molecular absorption. Due to the improved quality of many atmospheric spectroscopy instruments, the use of more sophisticated line shapes beyond Voigt, etc., might be necessary to model observed spectra correctly (see outlook in Section 5). Continuum corrections can have a significant impact on the spectrum, nb. for water [34,35]. Furthermore, collision-induced absorption (CIA [36]) can be important, especially in planetary atmospheres.

3. Implementation — GARLIC

GARLIC has been developed for high resolution atmospheric radiative transfer modeling with emphasis on efficiency, reliability, and flexibility. GARLIC is the modern Fortran (90/2008) re-implementation and extension of the MIRART (Modular InfraRed Atmospheric Radiative Transfer) Fortran 77 code [27,28] and is applicable for arbitrary observation geometry and instrumental SRF and FoV. In the transition phase (2007) every effort has been made to ensure that GARLIC and MIRART spectra (including intermediate quantities, e.g., cross sections) are (numerically) identical.

GARLIC serves a twofold purpose: the `garlic.f90` main program along with numerous subroutines is a pure simulation code, i.e. given the state of the atmosphere and an observation geometry the `garlic` executable computes atmospheric transmission and radiance, optionally convolved with appropriate instrument functions (SRF and FoV). Likewise in the Fortran 77 package MIRART, the pure simulation code was also known as SQuIRRL — Schwarzschild Quadrature InfraRed Radiation Line-by-line. On the other hand, the subroutines of `garlic.f90` comprise the core of forward models used in atmospheric inversion codes based on nonlinear least squares fitting. In this context, an additional challenge is the computation of derivatives of the spectrum with respect to the parameters to be fitted (the GARLIC approach will be further discussed in Section 3.6).

3.1. Voigt function computation

The convolution integral (7) defining the Voigt profile is conveniently expressed in terms of the Voigt function [31]:

$$g_\mathrm{V}(\nu-\hat{\nu},\gamma_\mathrm{L},\gamma_\mathrm{G})=\frac{\sqrt{\ln 2/\pi}}{\gamma_\mathrm{G}}K(x,y) \tag{9}$$

$$K(x,y)=\frac{y}{\pi}\int_{-\infty}^{\infty}\frac{\mathrm{e}^{-t^2}}{(x-t)^2+y^2}\mathrm{d}t \tag{10}$$

Here the dimensionless variables x, y are defined in terms of the distance from the line center $\hat{\nu}$ and the Lorentzian and Doppler half widths:

$$x=\sqrt{\ln 2}(\nu-\hat{\nu})/\gamma_\mathrm{G}\quad\text{and}\quad y=\sqrt{\ln 2}\gamma_\mathrm{L}/\gamma_\mathrm{G}. \tag{11}$$

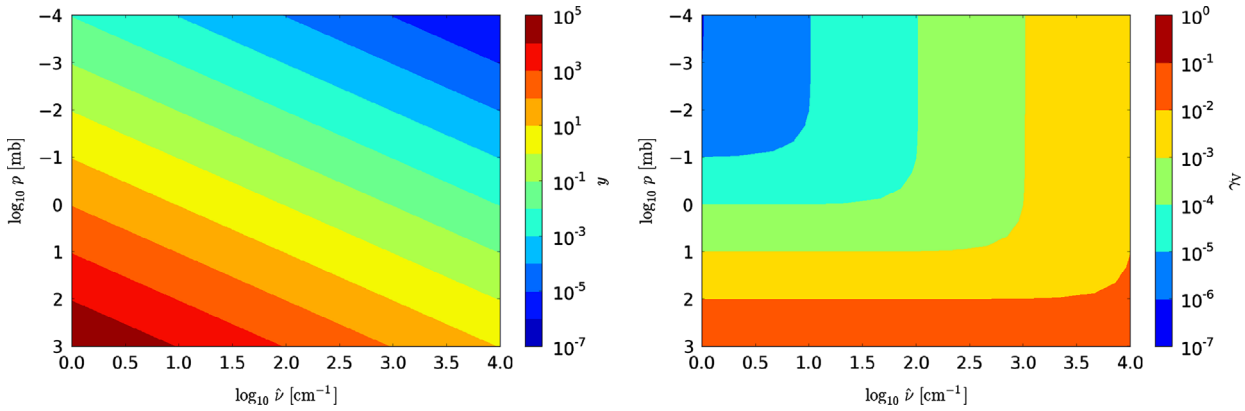

Fig. 1. Voigt parameters as a function of line position (essentially spectral region) and pressure (in mb): (a) the Voigt parameter $y=\sqrt{\ln 2}\gamma_L/\gamma_G$, and (b) the Voigt half width γ_V. Both variables were calculated assuming a reference pressure broadening half width $\gamma_L^0=0.1\ \text{cm}^{-1}/\text{atm}$, a molecular mass of 36 amu, and a mean atmospheric temperature of 250 K.

The half widths of the Voigt profile and the Voigt function are approximately given by [37]

$$\gamma_V(\gamma_L,\gamma_G)=\frac{1}{2}\left(\gamma_L+\sqrt{\gamma_L^2+4\gamma_G^2}\right) \tag{12}$$

$$x_{1/2}=\frac{1}{2}\left(y+\sqrt{y^2+4\ln 2}\right). \tag{13}$$

The Voigt function comprises the real part of the complex error function [38,39]:

$$w(z)\equiv K(x,y)+\mathrm{i}L(x,y)=\frac{\mathrm{i}}{\pi}\int_{-\infty}^{\infty}\frac{\mathrm{e}^{-t^2}}{z-t}\mathrm{d}t \tag{14}$$

with $z=x+\mathrm{i}y$. Unfortunately, neither the Voigt nor the complex error function can be evaluated in closed form and numerous algorithms have been developed with varying degree of accuracy and efficiency (cf. the review of Armstrong [31] or the comparisons [40–44]). Most modern algorithms rely on approximations for the complex error function; actually this approach has further advantages: because of the differential equation satisfied by the complex error function,

$$w'(z)=-2z\cdot w(z)+\frac{2\mathrm{i}}{\sqrt{\pi}} \tag{15}$$

it simultaneously provides derivatives of these functions required for, e.g., Hermite interpolation (see Section 3.2), sensitivity analysis, or optimization. Furthermore, the complex error function can be used if more sophisticated line profiles, e.g., the convolution of the van Vleck–Weisskopf (8) and Gaussian profile (6), the Rautian for collisional narrowing [45], speed-dependent line shapes [46], or line mixing effects, have to be computed (the latter are not yet implemented in the current version of GARLIC).

Rational approximations, i.e. the quotient of two polynomials

$$w(z)=\frac{P(\tilde{z})}{Q(\tilde{z})}=\frac{\sum_{m=0}^{M}a_m\tilde{z}^m}{\sum_{n=0}^{M+1}b_n\tilde{z}^n}\quad\text{where } \tilde{z}=y-\mathrm{i}x, \tag{16}$$

are known to enable accurate and efficient algorithms for a large class of functions, and have also been used to approximate the complex error function, e.g., Hui et al. [47], Humliček [48,49], Kochanov [50], and Weideman [51]. Because of the asymptotic behaviour of the complex error function ($w\sim 1/z$), the degree of the denominator is constrained to exceed the degree of the numerator by one. It should be noted that for atmospheric spectroscopy applications the Lorentz-to-Gauss width ratio varies over many orders of magnitude, i.e. $10^{-7}<y<10^4$, see Fig. 1a.

The Hui et al. [47], Kochanov [50] and Weideman [51] rational approximations appear to be quite tempting as they provide a single approximation applicable to the entire x,y plane. Unfortunately, however, $K(x,y)$ and $w(z)$ are especially difficult to evaluate for small y. In particular, the Hui et al. (with $M=6$) and Kochanov algorithms have significant accuracy problems for $y\ll 1$ and medium x, and the Weideman approximations require a large number of terms to achieve sufficient accuracy for small y, making it computationally less efficient (for a discussion of accuracy requirements, see, e.g., [52, Section 3.2]). Thus, in most algorithms the x,y plane (or the first quadrant $x,y\geq 0$ because of the symmetry relations) is divided into several regions and appropriate methods are utilized, e.g., a series approximation for small x,y and an asymptotic approximation for large x,y. The Humliček [49] code (or variations thereof, e.g., [53,54]) has been selected by several lbl codes (e.g., ARTS [25], GENLN2 [23], KOPRA [55], MOLIERE [56]), but its performance depends on the compiler's efficiency to handle nested conditional branches. (Actually, codes such as Humliček's can be processed in Fortran quite efficiently, but performance can be a serious issue for, e.g., Numeric Python.)

In order to avoid complicated `if` constructs for the calculation of the complex error function, GARLIC uses an optimized combination [52] of the Humliček [49] asymptotic approximation and the Weideman [51] expansion:

$$w(z)=\begin{cases}\dfrac{\mathrm{i}z/\sqrt{\pi}}{z^2-\frac{1}{2}}, & |x|+y>15\\[2ex] \dfrac{\pi^{-1/2}}{L-\mathrm{i}z}+\dfrac{2}{(L-\mathrm{i}z)^2}\displaystyle\sum_{n=0}^{N-1}a_{n+1}Z^n & \text{otherwise}\end{cases} \tag{17}$$

where $Z=(L+\mathrm{i}z)/(L-\mathrm{i}z)$ and $L=2^{-1/4}N^{1/2}$. The coefficients a^n of the Weideman expansion are characterized by a recurrence relation and can easily be obtained from an integral representation using a single Fast Fourier Transform. GARLIC uses $N=24$ what provides an accuracy better than 10^{-4} everywhere except for very small $y<10^{-5}$ and $4<x<15$ (hardly relevant in practise); for $N=32$ the relative error $|\Delta K|/K$ is less than 8×10^{-5} for all x,y of interest (see also [52, Fig. 8]).

3.2. "Multigrid" algorithm

Line widths depend on pressure and temperature (Fig. 1b), and generally lines become thinner with increasing altitude (until Doppler broadening starts to dominate). Thus, in GARLIC the uniform wavenumber grid is chosen individually for each altitude level and molecule, where the grid point spacing is determined by the half width:

$$\delta\nu=\gamma/\eta \quad \text{with } \eta=4.0 \text{ default.} \tag{18}$$

For the Lorentz line width, the mean (default) or the minimum width of all contributing lines is considered, and the Doppler width is estimated assuming a line positioned at the lower end of the spectral interval. For the Voigt profile width, the approximation (12) is used.

Even with a highly optimized Voigt function algorithm the (possibly) large number of function evaluations required for high resolution radiative transfer modeling (compare Fig. 1b) calls for further optimizations (for a discussion of requirements, see, e.g., Kohlert and Schreier [57]). Since the early days of lbl modeling a variety of techniques have been developed to reduce the number of Voigt function evaluations, cf. e.g., Clough and Kneizys [58], Edwards [23], West et al. [59], Gordley et al. [60], Fomin [61], Sparks [62], Titov and Haus [63], Kuntz and Höpfner [64], Kruglanski and De Mazière [65].

Most optimization schemes exploit the fact that the line shape varies rapidly only near the line center, whereas in the wings function values decrease slowly with increasing distance from the center. The Clough and Kneizys [58] approach was originally developed for the Lorentz profile and extended to the Voigt profile in FASCODE; in contrast, the Sparks [62] scheme is independent of the actual profile, but the series of grids with resolution doubled for each "tier" implies some computational overhead for the nested loops. In Schreier [66] an optimized algorithm using a sequence of three wavenumber grids with increasing resolution has been developed that does not make any assumptions regarding further properties of the line shape, nb. symmetry. Essentially, the line shape is decomposed in fast, medium, and slowly varying contributions to be evaluated on appropriate grids. After computation of the contributions from all relevant lines, Lagrange interpolation is used to "merge" the coarse and medium resolution superpositions back to the ultimate fine grid. Speed-ups of two-orders of magnitude with relative errors less than 10^{-3} have been realized.

Unfortunately, however, the use of Lagrange interpolation turned out to be problematic. Experience has shown that in rare cases four- or three-point Lagrange interpolation can introduce larger errors (or even negative cross sections). On the other hand, two-point interpolation is quite robust (and slightly faster), however the interpolation in the line wings always leads to an overestimate of the true function values (line profiles are convex in the wings; for typical error patterns of linear or quadratic interpolation see Fig. 3 in Schreier [66]).

To overcome these problems, a new approach utilizing cubic Hermite interpolation (e.g., [67,68]) has been implemented in GARLIC. The four coefficients of a polynomial of degree 3 are determined by the function values and the values of the first derivative at both ends of the interval to be approximated (see Appendix A). Because the Voigt function is computed as the real part of the complex error function, the derivative $\partial g_V/\partial\nu \propto \partial K/\partial x \propto xK-yL$ is easily available because of Eq. (15), thus this approach does not imply a higher computational burden compared to cubic Lagrange interpolation. Furthermore, this scheme can be readily adapted to other line shapes computed from the complex error function (e.g., [45,46]).

Apart from the line shape, the error of Hermite interpolation depends on the fine grid spacing $\delta\nu$ (see Eq. (18)), the coarse grid spacing $\Delta\nu$ (an integer multiple of $\delta\nu$), and the transition point ν_t from the dense to the coarse grid.

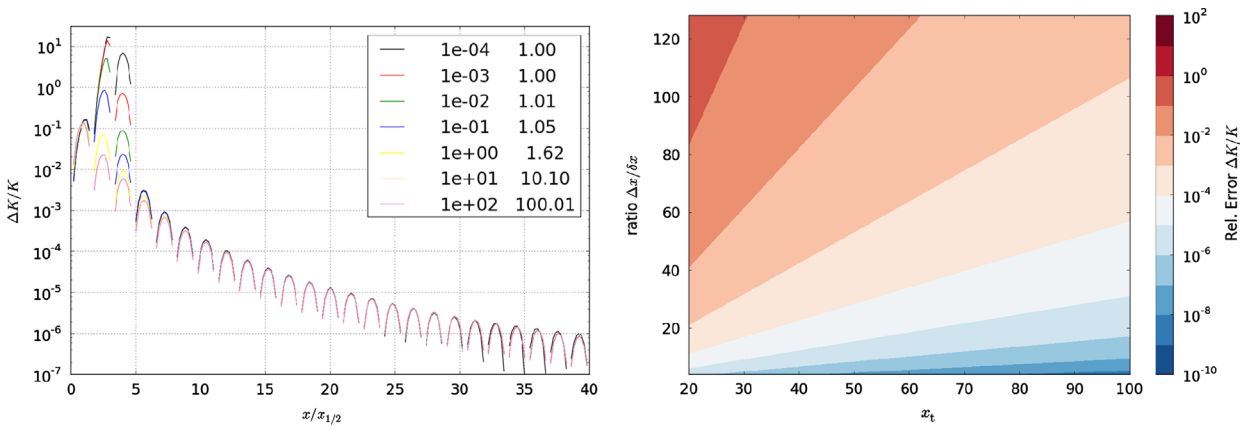

Fig. 2. Error of cubic Hermite interpolation for the Voigt function. Left: relative error for a coarse-fine grid point spacing ratio 8. The numbers in the legend box indicate y and $x_{1/2}$. Right: relative error at the center $x_t+\Delta x/2$ of the first interval evaluated on a coarse grid for $y=1$.

The relative error $\varepsilon \equiv (K_{\text{approx}}(x,y) - K_{\text{exact}}(x,y))/K_{\text{exact}}(x,y)$ for the Voigt function is shown in Fig. 2a for various y and a grid size ratio $\Delta x/\delta x = 8$ (where δx and Δx correspond to $\delta\nu$ and $\Delta\nu$, respectively, see (11)). Apparently, this error is almost independent of y what can be easily understood by employing the asymptotic expansion of the Voigt function (i.e. assuming $K(x,y) \approx (y/\sqrt{\pi})/(x^2+y^2)$ and neglecting y^2 in the denominator for $x \gg x_{1/2}$). The largest interpolation error is expected near the center of the first interval evaluated on a coarse grid, and in Fig. 2b the relative error is shown as a function of the transition point (in units of the half width, (13)) and the grid size ratio: for $\Delta x/\delta x = 32$ a coarse grid starting at about $|x| > 55x_{1/2}$ would ensure errors less than 10^{-4}. GARLIC uses grid ratios of 8, 16, and 32 for $y > 1$, $0.01 \le y \le 1$, and $y < 0.01$, respectively, in the line wings beyond $|\nu - \hat{\nu}| > 25\gamma$. Because the coarse grid is only used in the far wings, the large interpolation errors (essentially due to the use of the asymptotic approximation for the entire coarse grid) near the line center (Fig. 2a) are not a concern.

3.3. Parallelization/OpenMP

The previous two subsections discussed algorithmic approaches to speed up the time consuming computation of molecular cross sections. Exploiting hardware offers further possibilities to accelerate the code. Novel computing architectures [69] have gained attraction in recent years, and the potential of GPU's (graphics processing unit) and FPGA's (field programmable gate array) for lbl modeling has been studied by Collange et al. [70] and Kohlert and Schreier [57], respectively. However, the multi-core architecture of current CPUs allows parallelization without extra hardware accelerators, and OpenMP (see http://openmp.org/) has been chosen because of its ease-of-use and support for a variety of compilers.

Fig. 3 illustrates the implementation of the molecular cross section computation in GARLIC. Naively, one could choose to execute the loop over molecules in parallel, as these computations are largely independent. However, the number of spectral lines varies significantly from molecule to molecule. For example, in the 1000–1070 cm^{-1} interval (extended by $\pm 25\ \text{cm}^{-1}$) used for ozone retrievals from IASI (Infrared Atmospheric Sounding Interferometer [71]) observations there are 592 H_2O, 6856 CO_2, and 47 189 O_3 lines listed in the HITRAN 2012 database and the "water thread" would be idle for most of the time. Thus, the loop over levels has been selected as the "parallel region" to be executed by multiple threads and enclosed by the !$ `OMP PARALLEL` compiler directive. Note that the number of spectral points (`nFreqs`) is level depending and strongly increasing with altitude in the lower atmosphere (see Eq. (18) and Fig. 1b or [52, Fig. 2c]). Furthermore, the number of levels is not necessarily a multiple of the number of threads. Hence, before the next molecule can be processed, some threads will be idle until all levels have been done. Speed-ups of about a factor of five were achieved on a quadcore CPU with hyperthreading. Parallelization of further code segments, e.g., the radiative transfer for different wavenumbers or the limb sequence and FoV for different pencil beams, is planned.

```
DO m=1,nMolec
   read_hitrangeisa
   DO j=1,nLevels
      adjust_line_parameters
      DO l=1,nLines
         DO i=0,nFreqs
             xs += strength*voigtProfile
         END DO
      END DO
   END DO
END DO
```

Fig. 3. Pseudocode indicating the schematics of the molecular cross section computations.

3.4. Line strengths temperature dependence

The conversion of line strengths from temperature T_0, i.e. the reference temperature of the spectroscopic line parameter database, to the actual temperature T is calculated according to the scheme used in the ATMOS software [72]:

$$\frac{S(T)}{S(T_0)} = \frac{Q(T_0)}{Q(T)} \frac{\exp(-E_i/kT)}{\exp(-E_i/kT_0)} \frac{1-\exp(-hc\hat{\nu}/kT)}{1-\exp(-hc\hat{\nu}/kT_0)}. \tag{19}$$

Here, E_i is the lower state energy of the transition at $\hat{\nu}$, and $Q(T)$ is the product of rotational and vibrational partition functions, $Q = Q_{\text{rot}} \cdot Q_{\text{vib}}$ with

$$Q_{\text{rot}}(T) = Q_{\text{rot}}(T_0)\left(\frac{T}{T_0}\right)^{\beta}, \tag{20}$$

$$Q_{\text{vib}}(T) = \prod_{i=1}^{N} [1-\exp(-hc\nu_i/kT)]^{-d_i}, \tag{21}$$

where β is the temperature coefficient of the rotational partition function, and N is the number of vibrational modes with wavenumbers ν_i and degeneracies d_i. Data can be found in [72-74]. It should be noted that in the intercomparisons (Section 4.2) the use of different schemes to convert line strengths was discussed as one of the reasons for discrepancies between the codes.

3.5. Numerical solution of the Beer and Schwarzschild integrals

To compute the spectral radiance and transmission (or equivalently, the optical depth), the integrals in Eqs. (1) and (3) have to be discretized, because in general the atmospheric pressure, temperature, and concentration profiles are given only as a finite set of data points (with a typical altitude range up to about 100 km, e.g., Anderson et al. [75]). Furthermore, even if all profiles would be given analytically, a closed analytical solution of the integrals is unlikely to exist and hence would require a numerical approach.

A common approach is to subdivide the atmosphere in a series of homogeneous layers, each described by appropriate layer mean values for pressure, temperature, and concentrations. Using this "Curtis–Godson

approach" the total transmission $\mathcal{T}$ is the product of all layer transmissions, and the radiance is calculated recursively [23,76].

Obviously the integrals in Eqs. (1) and (3) can also be evaluated easily by application of standard quadrature schemes [67]; for example, using an n-point quadrature rule the optical depth in (3) is given generally by

$$\tau = \int_{s_b}^{s_e} \alpha(s)\,\mathrm{d}s = \sum_{j=1}^{n} w_j \alpha(s_j), \tag{22}$$

where s_j and w_j are the nodes and weights, respectively. GARLIC (or MIRART) has implemented a trapezoid quadrature scheme, the method of overlapping parabolas (implemented in the SLATEC routine `(D)AVINT`, [77, see Appendix B]), or a quadrature using the piecewise cubic Hermite interpolant of the integrand (based on the PCHIP package as part of SLATEC [67]). Note that these quadrature rules work for arbitrarily spaced (i.e. not necessarily equidistant) abscissas s. For a close to vertical path with zenith angle ϑ in a flat plane-parallel atmosphere the altitude grid points z_l and the path grid points s_j are essentially equivalent except for a $\cos(\vartheta)$ factor. For limb path geometries a mapping of the altitude dependent atmospheric profiles to the distance s along the line of sight is performed, e.g., $T(s) = T(z(s))$.

As indicated in Eqs. (1), the Schwarzschild equation can be written in three mathematically equivalent variants, i.e. the integrals can be performed using the path distance s, optical depth τ, or transmission $\mathcal{T}$ as integration variable. GARLIC uses optical depth τ as integration variable, cf. Eq. (1b). To improve the numerical performance of the trapezoid quadrature scheme, a variant called "trapezoid-Laguerre quadrature" has been implemented, i.e. the Planck function is approximated by a linear function in τ and the resulting integrand $(b_0 + b_1\tau)\mathrm{e}^{-\tau}$ is evaluated exactly, see Appendix C. In addition to this "B linear in optical depth" scheme (default), GARLIC also offers a "B exponential in optical depth" approach, where the Planck function within a layer $\tau_l \le \tau < \tau_{l+1}$ is approximated by $B(T(\tau)) = B(T(\tau_l))\,\mathrm{e}^{\beta(\tau-\tau_l)}$, see Appendix D and [78]. (Alternatively, this approach can be seen as a linear interpolation of the logarithm of $B(\tau)$.)

In view of the (approximately) exponential decrease of pressure with altitude, it would be tempting to use the trapezoid-Laguerre quadrature also for evaluation of the optical depth integral (22). However, for a single absorber the integrand is the product nqk of air density n (proportional to pressure), volume mixing ratio q, and cross section k. For molecules with constant mixing ratio (e.g., CO_2 on Earth, Mars and Venus) trapezoid-Laguerre quadrature might be useful, but for other molecules mixing ratios can be strongly increasing or decreasing with altitude, so that the integrand is not proportional to an exponential. Furthermore, the cross section is also strongly altitude dependent, and this dependency varies with wavenumber: assuming a single Lorentzian line, the cross section is proportional to pressure in the line wings, and proportional to the reciprocal pressure in the line center. For these reasons, GARLIC uses a standard trapezoid scheme.

3.6. Jacobians by automatic differentiation

Jacobians, i.e. derivatives with respect to temperature, molecular concentrations or other variables relevant for atmospheric remote sensing, are important for sensitivity studies and mandatory for the solution of inverse problems formulated as nonlinear least squares typically solved by Newtonian iteration based on linearization.

In many cases the differentiation to compute the Jacobian is performed by finite difference numerical derivatives, and thus frequently constitutes the most time consuming part of the retrieval. More seriously, the appropriate amount of perturbation is difficult to predict (truncation and/or cancellation errors, see [79]). Even worse, in case of molecular concentration derivatives, the proper change is dependent on wavenumber: in spectral regions with strong absorption due to the molecule under consideration a small change might be sufficient, whereas in regions of weak absorption a large change will be necessary to see a noticeable change in the radiance or transmission. Likewise, a different temperature sensitivity of different spectral regions demands for a careful selection of the temperature perturbation.

Analytical means of derivative calculations are therefore advantageous, both for computational efficiency and accuracy, and accordingly several codes developed with (operational) retrieval applications in mind implement analytically derived Jacobians, e.g., ARTS, FORLI, KOPRA, LBLRTM, MOLIERE, σ-IASI [24-26,55,80–82]. However, calculating derivatives manually and implementing these in a moderately large code are tedious and error prone. Furthermore, any updates in the pure forward code are not automatically "propagated" to the derivative code.

Automatic (or algorithmic) differentiation (AD) provides a pleasant alternative to quickly generate derivative-enhanced versions of computer codes which is rarely used in atmospheric remote sensing. Automatic differentiation techniques [83,84] are based on the fact that every model implemented as a computer program is essentially formulated in a sequence of elementary operations (sums, products, powers) and elementary functions. In contrast to integration, differentiation is based on a few simple recipes such as the chain rule, and these can be performed automatically by some kind of precompiler, taking a computer code as input and delivering a code that additionally produces derivatives with respect to some chosen variables. A number of automatic differentiation tools are available for Fortran, C, etc. (cf. the compilation given at http://www.autodiff.org/). It should be noted that AD generates "exact" derivatives, i.e. there are no approximations introduced during code generation.

In the Fortran 77 MIRART package [27] derivatives had been implemented utilizing the source-code transformation ADIFOR [85]. The retrieval codes built on GARLIC, e.g., BIRRA and PILS [86,87], utilize the source-to-source AD tool TAPENADE (version 3.4) [88] to generate derivatives in forward (tangent) mode. For a discussion of the pros and cons of the various AD techniques, see, e.g., Bischof and Bücker [89].

Fig. 4 clearly indicates the problem of choosing the right perturbation for finite difference approximations.

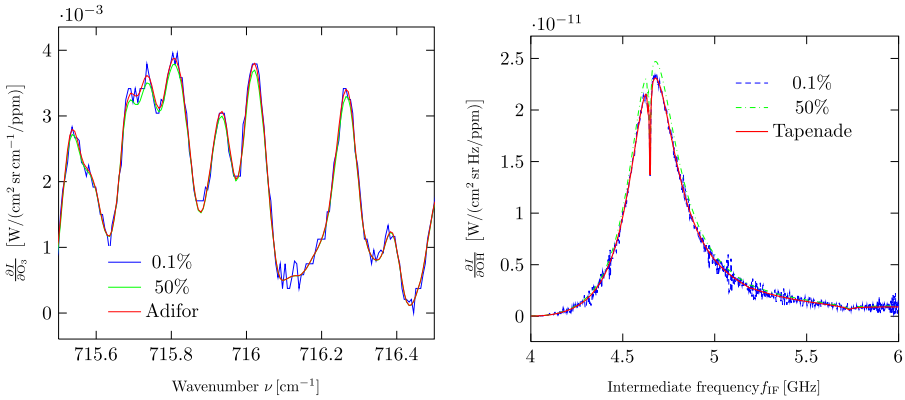

Fig. 4. Automatic differentiation versus finite difference: (a) comparison of partial derivatives of the radiance (limb view with 12 km tangent altitude) with respect to O_3 volume mixing ratio at 21 km in a MIPAS-Envisat configuration. (b) comparison of partial derivatives with respect to OH volume mixing ratio in a typical OH frequency microwindow; the derivatives are evaluated at an altitude level of 21 km for a tangent altitude of 19 km and an balloon-borne observer at 35 km.

Fig. 4a shows Jacobians typical for data processing of spaceborne thermal limb emission sounders such as MIPAS [90]. Using ADIFOR the time required to evaluate derivatives of 11 radiance spectra comprising the limb sequence with respect to the ozone volume mixing ratio (VMR) at 32 altitude levels is increased by a factor of 2.4 compared to the time required for the 11 spectra alone. The spectra in the 13.95–13.98 μm range were evaluated with three absorbers (H_2O, CO_2, O_3 including continuum) assuming a Gaussian FoV and a sinc SRF. For the 12 km tangent radiance spectrum differentiated w.r.t. ozone at 21 km, the finite differences spectra clearly oscillate around the exact derivative spectra, with some derivative values evaluated to zero for the 0.1% perturbation.

In Fig. 4b, one column of the Jacobian matrix (derivative w.r.t. OH VMR at 21 km) for a typical double sideband frequency window of the 1.8 THz channel computed with the derivative code given by TAPENADE and by the finite difference method (evaluated with 0.1% and 50% perturbation) is compared. (Double sideband instruments like TELIS (see Section 4.3.1) record the superposition of spectra covering two frequency domains to the left and right of the local oscillator frequency f_{LO}, the intermediate frequency f_{IF} is the difference between absolute frequency $f = c\nu$ and the local oscillator frequency.) The 0.1% perturbation finite difference shows significant oscillations, whereas the 50% perturbation finite difference has a clear offset compared to the exact derivative. The total computation time for all spectra comprising an entire limb sequence of 10 tangent altitudes plus Jacobians for 23 altitude levels is increased by just a factor of 2 in contrast to the pure forward calculation. Note that for a level-based scheme as used by GARLIC, differentiation corresponds to a triangular disturbance centered at the target altitude level, cf. Hase et al. [91].

In order to generate derivative code with tools like ADIFOR or TAPENADE it is necessary to select an appropriate subroutine (the "top-level subroutine" in ADIFOR's notation) and all subroutines called by this routine. In case of molecular concentration retrievals from thermal emission spectra, this set of routines will comprise code for the evaluation of the Schwarzschild integral along with routines to model instrument effects (SRF and FoV), the input for the top-level routine, say `schwarzschild_instrument`, will consist of atmospheric data (pressure, temperature, concentration) along with geometric and instrumental parameters, and the output will be the radiance array. ADIFOR and TAPENADE allow the user to request derivative code generation for several of the top-level subroutine's input arguments (e.g., the molecular concentration and some "auxiliary" parameters to be fitted simultaneously). However, in case of the retrieval codes based on GARLIC, all fit variables are packed in a single array `X` before calling the top-level subroutine, and unpacked to the "physical" variables inside this routine. This approach has been chosen because a single state vector array `X` is also required as an argument to typical least squares solvers; furthermore a single input argument slightly simplifies the generation of the derivative code with TAPENADE. It should be noted that the elements of the input vector for which derivatives are to be computed can be selected at run-time using the so-called "seed matrix".

3.7. Viewing geometry

All observation geometries relevant for atmospheric remote sensing are supported by GARLIC. For up and limb viewing geometries, refraction of the line-of sight is modeled optionally following the approach used in MOLIERE [81]. For nadir viewing, reflection of downwelling radiation at the surface can be taken into account (e.g., [80]) where the solar (or exoplanet's host star) irradiance is taken as a simple Planck blackbody source or from data such as Chance and Kurucz [92]. FoV spectra are evaluated as a sequence of pencil beam spectra and subsequent convolution with an appropriate FoV function.

As discussed in Section 3.5, GARLIC evaluates the path integral equations (1) and (3) using numerical quadrature schemes where the quadrature nodes correspond to the altitude levels of the discrete atmospheric data. In case of limb sounding the tangent point could be located between two altitude levels; in order to improve the integral evaluation an additional path grid point at the tangent is

added with temperature and absorption coefficient values obtained by linear interpolation. For up- or downlooking geometries, observer or path end points at altitudes not coinciding with altitude grid points are treated in a similar fashion.

3.8. Input files and job execution

One of the fundamental design principles of GARLIC (and MIRART) has been a strict separation between code and data. Accordingly, only a few mathematical and physical constants are specified in the code, e.g., π, $\sqrt{\ln 2}$, speed of light c, Boltzmann's constant k, and Planck's constant h. Any further data, nb. molecular parameters such as mass and HITRAN, GEISA, etc. identification codes, atmospheric state parameters (pressure, temperature, composition), and molecular spectroscopic data (line parameters) are read from external files. (Unfortunately, it was not possible to adhere to this principle for the continuum implementation because of several "fudge factors", etc.) This clear separation of code and data greatly facilitated the application of MIRART/GARLIC to other planets' atmosphere.

Molecular cross sections are calculated with spectroscopic data from HITRAN [18], HITEMP [19], GEISA and GEISA/IASI [32,33], or JPL [93] dataset(s) (with units as used in HITRAN/GEISA, e.g., cm^{-1} for line positions and energies, and $\mathrm{cm}^{-1}/(\mathrm{molecule\,cm}^{-2})$ for line strength). Alternatively, precalculated cross sections can be read from external files. In addition to the line contributions, continua are implemented for water, carbon dioxide, oxygen, and nitrogen [34,94], where a "Voigt-CKD" line shape is used in conjunction with the CKD continuum with a cut-off wavenumber of $25\,\mathrm{cm}^{-1}$ and subtraction of the line wing value. Furthermore, collision-induced absorption [95,96] for a variety of collision pairs can be considered, too.

In its present version, GARLIC considers only one-dimensional atmospheres with profiles given as a function of altitude, e.g., the AFGL dataset [75]. Data from several sources and with different discretization and different physical units (internally GARLIC uses cgs units consistently) can be mixed, and the altitude grid of the first profile read defines the final grid used for the computation. This approach is especially convenient for retrieval applications: because of the ill-posed nature of the inverse problem, a coarse resolution of the profile to be fitted is frequently justified (thus limiting the size of the state vector; a finer grid would be compensated by stronger regularization, e.g., smoothing, anyway), whereas a fine altitude resolution is required for the radiative transfer (forward) modeling. Accordingly, the retrieval codes based on GARLIC typically read all known profiles first on a fine grid before reading the (current estimate of the) profile(s) to be fitted on a coarse grid. For example, in case of molecular concentration profile retrievals pressure, temperature and concentration of interfering gases are read first on a dense grid (e.g, the AFGL profiles), before the profile of the molecule of interest is read and interpolated from the coarse retrieval grid to the fine forward model grid.

GARLIC proceeds essentially in two steps: first cross sections of all molecules considered are computed for all atmospheric levels and then summed up to the absorption coefficients (optionally with continuum corrections). In a second step the radiative transfer (essentially Beer's and Schwarzschild's equation) is evaluated for one (or several) path(es) with temperature and absorption coefficients as input along with geometry. This separation of computing the extinction properties and the radiative transfer is possible because of the level-based approach combined with numerical quadratures and avoids time-consuming recalculation of cross sections for each line-of-sight.

4. Evaluation, verification and validation

One of the most important, yet difficult steps in program development is an extensive code testing, i.e. careful check of the program performance. Unfortunately, a closed analytic solution of the radiative transfer equations is not available for realistic conditions, and hence a comparison of numerical results with reference values is not feasible. Clearly, testing code against analytical results is mandatory for intermediate quantities, e.g., cross sections composed of a small number of lines for a particular pressure, temperature, and molecule, but this obviously does not prove the correctness and consistency of the whole code. Comparing computed spectra with experimental measurements is difficult due to the incomplete knowledge of the atmosphere (i.e. pressure, temperature, and composition of a generally inhomogeneous medium), inaccuracy of spectroscopic data, and possible distortions by instrumental artifacts. Thus this approach is essentially limited to laboratory measurements for a homogeneous gas cell, i.e. it does not test the correctness of the numerical solution of the path integrals in Eqs. (1) and (3). Historically, the lbl routines used in GARLIC/MIRART are largely based on routines used in the FitMAS (Fit Molecular Absorption Spectra) code for nonlinear least squares fitting of spectroscopic line parameters to high resolution molecular spectra. FitMAS has been cross-checked with similar codes [97,98] and is used extensively for analysis of our institute's (DLR) Fourier transform spectra (e.g., [99]). Likewise, proper implementation of the spectral response can be validated by means of laboratory spectroscopy.

Verification and validation are established as mandatory in computational science [100]. According to Post and Votta [101], verification determines that the code solves the chosen model correctly, whereas validation tries to confirm that the model captures the physics correctly. In a detailed analysis, Boisvert et al. [102] discussed the road from the real world via the mathematical model and computational model to the computer implementation and accordingly distinguish between code verification and solution verification in addition to validation. In the context of atmospheric radiative transfer modeling, the Schwarzschild and Beer equations, (1) and (3), can be viewed as the mathematical model; the need for discretization of the continuous variables leads to the computational model approximating the integrals by finite sums, e.g., Eq. (22) according to an appropriate quadrature

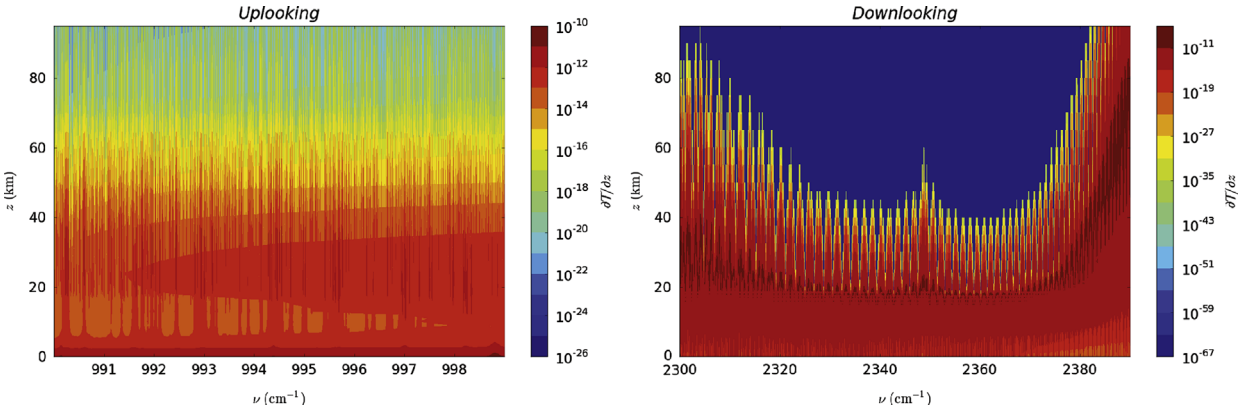

Fig. 5. Weighting functions $\frac{\partial \mathcal{T}}{\partial z}$. Left: uplooking geometry, ozone 9.6 μm band; Right: downlooking geometry, carbon dioxide 4.3 μm band.

scheme, that is finally implemented in a Fortran (or any other language, C/C++, Python, etc.) code.

Verification of computer codes is frequently performed by careful intercomparisons of similar codes, and for radiative transfer models in particular such tests have been the focus of a growing number of workshops and reports, e.g., Fischer et al. [103], Ellingson and Fouquart [104], Soden et al. [105], Garand et al. [106], von Clarmann et al. [29], Tjemkes et al. [107], Kratz et al. [108], Melsheimer et al. [30]. Attempts to validate lbl codes by comparison of model vs. observed spectra accompanied by careful characterization of the state of the atmosphere (closure experiments) are presented in, e.g., Strow et al. [109], Masiello et al. [110], Newman et al. [111] or Buehler et al. [112].

In the next subsection, we discuss the performance of the various quadrature schemes presented in Section 3.5 as an approach to code verification. Solution verification by intercomparison with independently developed codes is the topic of Section 4.2, and Section 4.3 shows validation results by comparing synthetic spectra with observed spectra.

4.1. Comparison of quadrature schemes

From a numerical point of view, the evaluation of the integrals in Eqs. (1) and (3) is probably the most delicate step of infrared radiative transfer modeling. Having selected an appropriate line shape and given an accurate algorithm, the lbl computation is essentially an efficiency problem. Likewise, computing the absorption coefficient is basically a series of array operations (SAXPY, i.e. scalar multiplication and vector addition "aX+Y"), and the continuum correction is to a large extent a "physical" problem of data and their proper parameterization. Moreover, for lbl cross sections (and continuum alike) a critical problem is data quality, i.e. the availability of good input data. Hence, those aspects of radiative transfer modeling concerned with the spatial variability of the atmosphere (i.e. the path quadratures) are the most difficult to assess.

As already indicated, Eqs. (1) represent three mathematically equivalent solutions of the differential radiative transfer equation. However, all of these forms have problems for numerical quadrature rules. For Eq. (1a), the path distance s_j ($j=0,1,2,\ldots$) grid points are usually of the same order of magnitude, with grid points more or less equally spaced. However, the transmission $\mathcal{T}$ and absorption coefficient α factors can vary over many orders of magnitude. Note that for uplooking geometry both factors are essentially exponentials decreasing with increasing altitude, whereas for downlooking geometry $\mathcal{T}$ decreases with decreasing altitude (see the sketch in [3, Fig. 11.9]). Accordingly, the product of these two factors, the weighting function $\partial\mathcal{T}/\partial z$ (originally introduced in the context of spaceborne temperature sounding for meteorology and planetary science) varies over many orders of magnitude, see Fig. 5. Similarly, the optical depth in Eq. (1b) can vary significantly in magnitude, and the same is true for the transmission $\mathcal{T}$ in Eq. (1c). In contrast, in the thermal infrared the Planck function $B(\nu,T)$ increases by less than a factor four for temperatures rising from 200 to 300 K (in the microwave regime the Planck function is proportional to temperature according to the Rayleigh–Jeans law).

As discussed in Section 3.5 GARLIC generally uses optical depth as integration variable, i.e. Eq. (1b). For the comparisons shown here, a trapezoid quadrature for Eq. (1a) has been implemented additionally. The top row in Fig. 6 shows the upwelling radiation in the spectral region around 9.6 μm typically used for ozone remote sensing by nadir sounders such as AIRS (Atmospheric Infrared Sounder [113]), CrIS (Cross-track Infrared Sounder [114]), IASI [71], or TES (Tropospheric Emission Sounder [115]). The spectrum has been calculated with the trapezoid-Laguerre scheme using an atmosphere specified at 121 equidistant altitude levels up to 120 km (denoted as "TL121", data taken from the AMIL2DA intercomparison [29], cf. next subsection). Monochromatic and spectra convolved with a sinc function (with a maximum optical path difference of 2 cm) are shown in the left and right columns, respectively.

The second row shows the relative difference $(I-I_{\mathrm{TL121}})/I_{\mathrm{TL121}}$ of the exponential-in-opticalDepth, cubic Hermite, and trapezoid path-distance quadrature (the SLATEC overlapping parabola routine `DAVINT` fails for some spectral points and is not shown here). The quadratures based on the Planck-linear-in-opticalDepth and Planck-exponential-in-opticalDepth perform equally well (deviations less than 0.04%), whereas deviations for

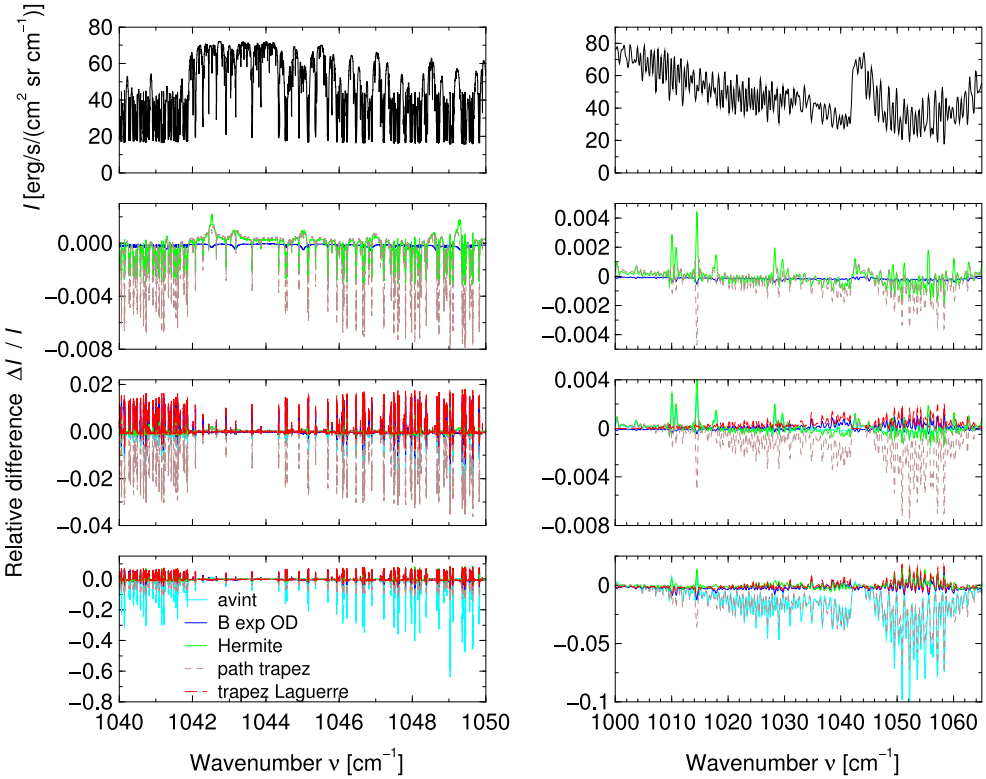

Fig. 6. Radiance in the ozone band for a nadir view from space. Left: monochromatic high resolution spectra; Right: spectra convolved with an ILS for a Fourier transform spectrometer with MOPD = 2 cm. The top row shows radiance computed with trapezoid-Laguerre quadrature for the 121 level atmosphere (TL121). The lower rows show relative differences with respect to TL121 for 121, 50, and 24 levels.

Hermite or trapezoid path-distance quadratures are a magnitude larger.

Obviously, a dense discretization with 121 equidistant levels is computationally demanding and the appropriate choice of a coarser vertical discretization has been discussed by, e.g., Hase et al. [91] or Wiacek and Strong [116]. The third and fourth rows give relative differences to TL121 for quadratures using 50 (equivalent to the "AFGL grid" [75]) or 24 levels. Note that linear interpolation errors for the 50 level temperature profile are about 0.1 K except for two peaks with $\Delta T \approx -0.46$ and 0.2 K at 48 and 32 km, whereas errors are as large as 3.2 K for the 24 level temperature. However, weighting functions (e.g., [117]) indicate that the radiation is originating predominantly from the troposphere or lower stratosphere. Clearly, trapezoid path-distance or overlapping parabola quadrature has the largest deviations, for high and low resolution spectra and for all altitude discretizations. The overlapping parabola quadrature, as implemented in SLATEC's `DAVINT` routine, fails in some cases and is also not recommended for practical usage. For the 24 level atmosphere, the trapezoid-Laguerre and exponential-in-opticalDepth spectra have deviations less than 2% from the TL121 reference spectrum (less than 0.2% for the 50 level atmosphere). This might be considered as acceptable in view of the computational savings, however, investigation of the corresponding equivalent brightness temperature differences (Fig. 7) indicates deviations of about half a Kelvin what is about the noise level of the IASI instrument aboard MetOp.

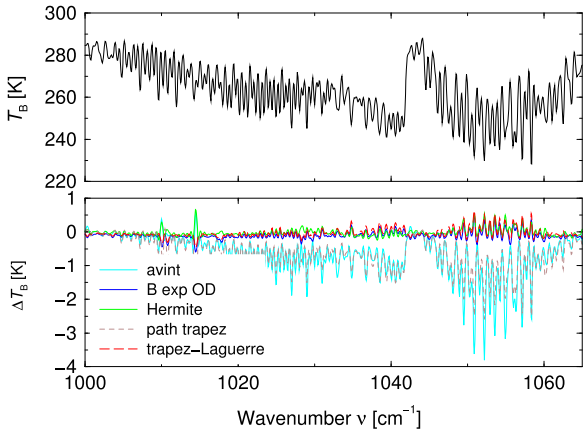

Fig. 7. Top: Equivalent brightness temperature in the ozone band for a nadir viewing geometry (Spectra convolved with an ILS for a Fourier transform spectrometer with MOPD = 2 cm). Bottom: brightness temperature differences $T - T_{\mathrm{TL121}}$ for 24 level atmosphere versus 121 level trapezoid-Laguerre.

Concerning computational speed, `DAVINT` and `PCHIP` are significantly slower than the other quadrature schemes (the overlapping parabola quadrature can be easily optimized, but this does not improve its robustness). In case of the exponential-in-opticalDepth scheme care has to be taken for layers with identical lower and upper temperatures or optical depth. In view of these

considerations, GARLIC uses the trapezoid-Laguerre rule for optical depth as integration variable as default method.

4.2. Verification — code intercomparison

A standard approach to solution verification of lbl codes relies on cross-checking against similar codes. In the last decade MIRART has participated in two extensive intercomparisons, and currently an intercomparison of GARLIC with ARTS (Atmospheric Radiative Transfer Simulator [25,26]) and KOPRA (Karlsruhe Optimized & Precise Radiative transfer Algorithm, [55]) is being performed (see [118], for preliminary results). Some of the tests of the MIRART–KOPRA and MIRART–ARTS intercomparisons have been repeated with GARLIC and the results are presented in the following subsections. In both studies, some of the deviations of MIRART from the reference code were attributed to the different line strength conversion schemes and different CKD continuum versions. Both studies concluded that in general the "overall interconsistency" of the spectra provided by the various models is good. However, considerable discrepancies were found when models used different settings or assumptions with respect to numerical accuracy, algorithms, or input data.

4.2.1. AMIL2DA

In order to assess the consistency of geophysical data (level 2) generated from measurements (level 1) by the MIPAS Fourier transform limb emission spectrometer onboard the ENVISAT satellite [90], the AMIL2DA (Advanced MIPAS Level 2 Data Analysis) project aimed at careful comparison and characterization of algorithms and data analysis strategies used by five different European groups. An essential step of this project was a cross comparison of the radiative transfer to be used as forward models in the group's MIPAS data processing [29]. The intercomparison was organized as a series of exercises, starting from simple settings proving basic functionalities and proceeding to more complex and realistic scenarios. Accordingly, the first exercises considered the cell transmission (i.e. a homogeneous atmosphere) of a single N_2O line for different pressures and temperatures, hence testing line shape computation, line strength conversion, and spectral response convolution.

In a second set of exercises, radiance spectra for a limb viewing geometry with instrumental effects (FoV, ILS) have been intercompared. Exercise 20 has been set-up to test the integration of the radiative transfer equations and the FoV convolution for a high tangent point where refraction is not an issue. Fig. 8 shows a comparison of KOPRA and GARLIC limb emission spectra, revealing deviations well below 1%. Trapezoid path-distance quadrature deviations are about a factor two larger than the differences for Planck linear or exponential in optical depth. Furthermore, it can be noted that the change in the spectroscopic database (from HITRAN 98 to HITRAN 2012) leads to significantly larger differences.

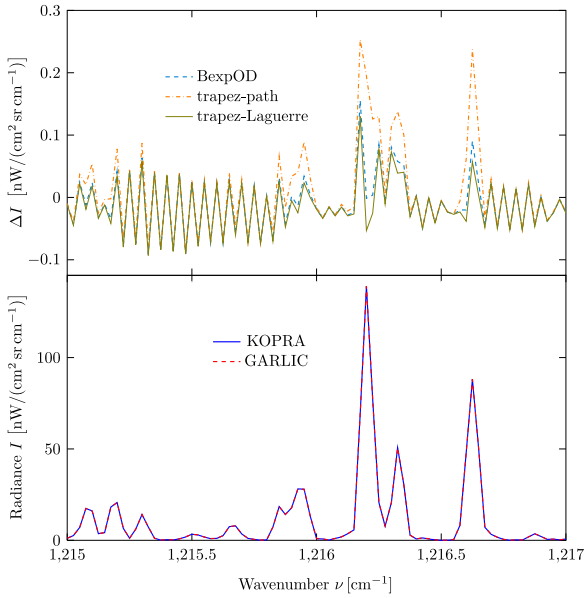

Fig. 8. AMIL2DA forward model intercomparison (Exercise 20): KOPRA line-by-line code [55] and GARLIC. Limb view with tangent altitude 40 km, apodized FTS instrument line shape, finite field-of-view, H_2O, CO_2, O_3, N_2O, and CH_4; HITRAN 98 (an update of HITRAN 96 developed for MIPAS data analysis), CKD-continuum [34]. Bottom: Radiances KOPRA vs. GARLIC; Top: Radiance differences $\Delta I = I_{\mathrm{KOPRA}} - I_{\mathrm{GARLIC}}$.

4.2.2. IRTMW01

A major objective of the Third International Radiative Transfer Modeling Workshop 2001 — IRTMW01 was the intercomparison of eight radiative transfer codes in the microwave spectral domain [30]. Similar to the AMIL2DA intercomparison, it was organized in a series of progressively more sophisticated "cases", starting with an assessment of Voigt line shape and molecular absorption coefficient calculations. As for the corresponding AMIL2DA exercises, MIRART exhibited slight deviations for spectra at temperatures different from the database reference temperature, which have been attributed to the use of different line strengths conversion approaches. (ARTS uses the TIPS — Total Internal Partition Sum [119] scheme for "HITRAN molecules".)

The purpose of case 3 was to check the correct implementation of the radiative transfer algorithm, nb. the solution of the integrals in Eqs. (1) and (3) (i.e. code verification). In order to allow to discriminate different sources of possible deviations between the models, absorption coefficients $\alpha(\nu, z)$ were precalculated with ARTS by the University of Bremen group and used as common input. Two sets of data have been provided by Bremen on a coarse grid with 45 levels and a fine grid with 264 levels used as benchmark. Case 4 tested the entire computational chain of the codes including lbl calculation, continuum corrections, and path quadrature. Geometries and instrument settings were identical to case 3, thus changes from case 3 spectra to case 4 spectra have to come from differences in the input data or from differences in the cross section and absorption coefficient calculations. The intercomparison was performed for all geometries (including limb, not shown here), and for ideal monochromatic spectra as well as ILS and FoV convolved spectra. Cases 3 and 4 downlooking essentially mimicked a microwave temperature sounder like AMSU-B (Advanced Microwave Sounding Unit) with three absorbers (O_2, H_2O,

and N_2), whereas cases 3 and 4 uplooking corresponds to an airborne trace gas sounder (with two active species, O_3 and O_2).

Figs. 9 and 10 show monochromatic spectra for the downlooking and the uplooking geometry, respectively. For the new GARLIC simulations shown here, only the coarse grid data was considered since for this atmosphere the integrals are more sensitive to the quadrature method. For the uplooking case, differences to ARTS (version 1-0-64) are in the sub-Kelvin range except for overlapping parabola quadrature and trapezoid path-distance quadrature. Except for the trapezoid path-distance scheme this is also true for the downlooking case. The comparisons essentially confirm the conclusions of Section 4.1, i.e. the choice of the trapezoid-Laguerre quadrature scheme as the default method because of its accuracy and speed.

4.3. Validation

4.3.1. Far infrared limb sounding — TELIS

For the analysis of limb observations, the program PILS — Profile Inversion for Limb Sounding — has been developed combining a forward model built from GARLIC's subroutines with a nonlinear least squares solver based on the PORT library [120,121]. To cope with the ill-posed inverse problem, PILS uses a variety of Tikhonov-type regularization methods. Currently, PILS is mainly used for the retrieval of stratospheric trace gas profiles from TELIS

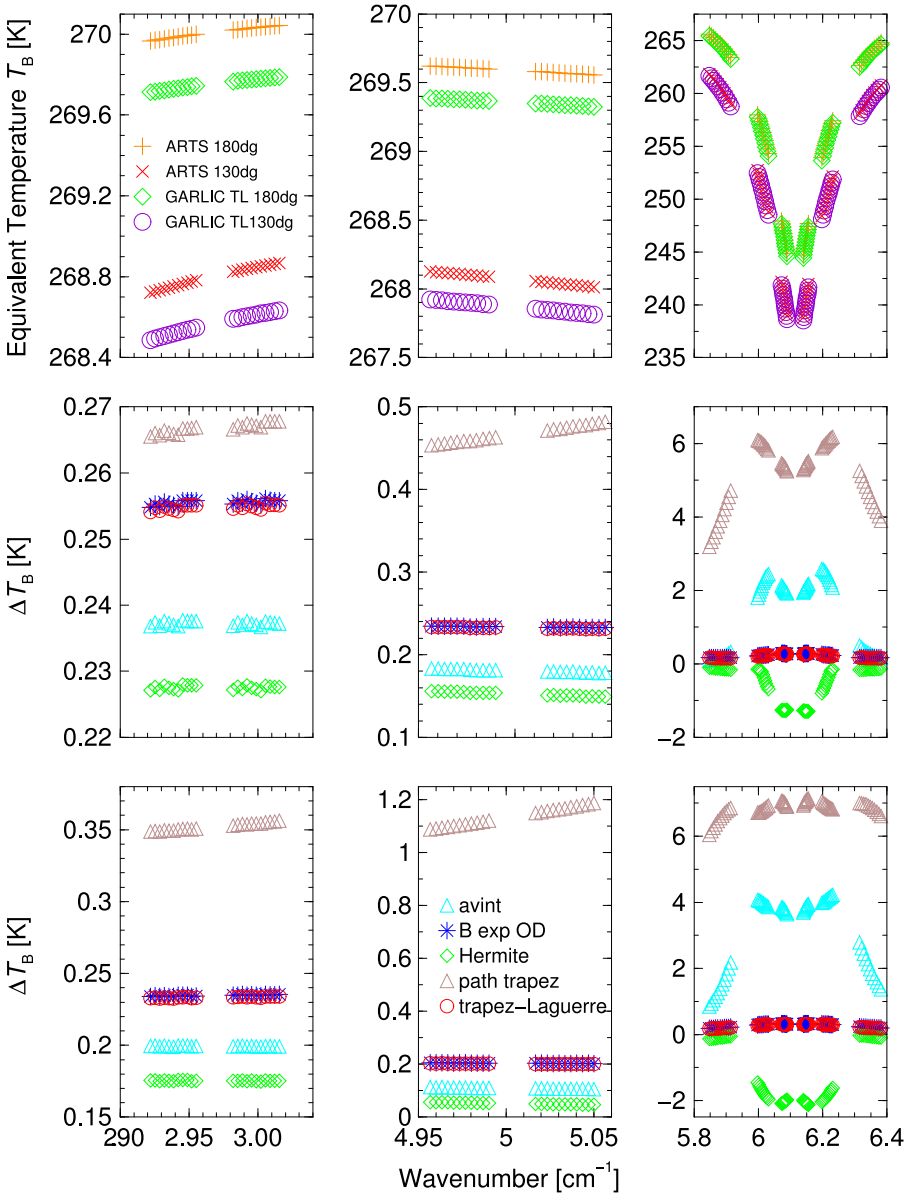

Fig. 9. IRTMW01 intercomparison ARTS vs. GARLIC: case 3 down-looking (monochromatic, coarse atmosphere). The second and third row depict the brightness temperature differences for 180° and 130°, respectively.

(TErahertz and submillimeter LImb Sounder), a balloon-borne cryogenic heterodyne spectrometer with two far infrared and sub-millimeter channels (1.8 THz and 480–650 GHz developed by DLR and SRON, respectively), but it can be used for other instruments such as SMILES or MIPAS (For a comparison of PILS' Fortran 77 predecessor based on MIRART with other codes in the context of the AMIL2DA project, Section 4.2, see von Clarmann et al. [122]). PILS allows to retrieve the discretized profiles of one or several trace gases from single or multiple micro-window limb sequences. In this context, fitting of an altitude dependent "grey-body" profile (i.e. a frequency independent additive correction of the absorption coefficient) turned out to be important in order to compensate for imperfect knowledge of continua (water, clouds, etc.) as well as pointing (e.g., [6]). The comparison of the model spectra with and without this additional grey-body and the observed spectra in Fig. 11 clearly demonstrates the impact of this approach, removing the high bias over the ozone lines for the lower tangent altitudes and ultimately leading to significantly reduced residuals.

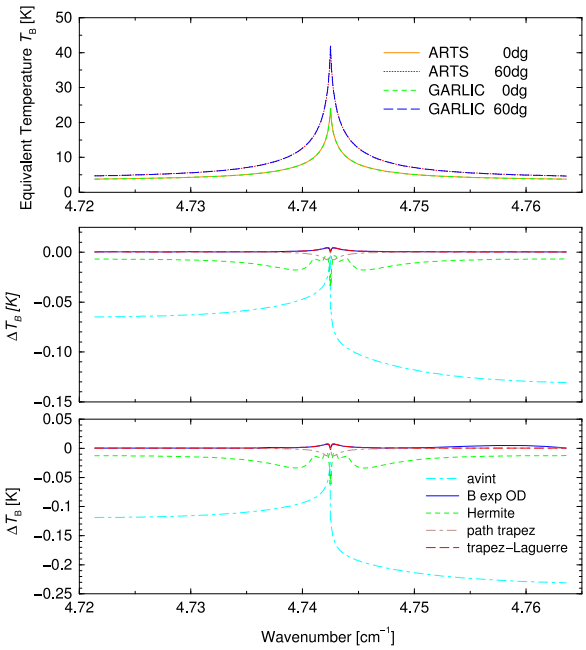

Fig. 10. IRTMW01 intercomparison ARTS vs. GARLIC: case 3 up-looking from an altitude of 10 km (airborne observer, monochromatic, coarse 45 level atmosphere) The second and third row show differences for 0dg and 60dg, respectively.

4.3.2. Thermal infrared nadir sounding: AIRS

Biomass burning (wildfires, etc.) and volcanic eruptions are of major concern both on a global (climate change) and regional (air pollution) scale. Accordingly, observation and monitoring of these high temperature events by space-borne instruments is highly desirable. Currently, there is no dedicated mission or sensor in orbit, but airborne sensors have been used successfully to demonstrate the feasibility [123].

Although current operational thermal IR nadir sounders are not optimized for biomass fire remote sensing, we have analysed AIRS observations over Portugal, August 2003, where large wildfires contributed significantly to the

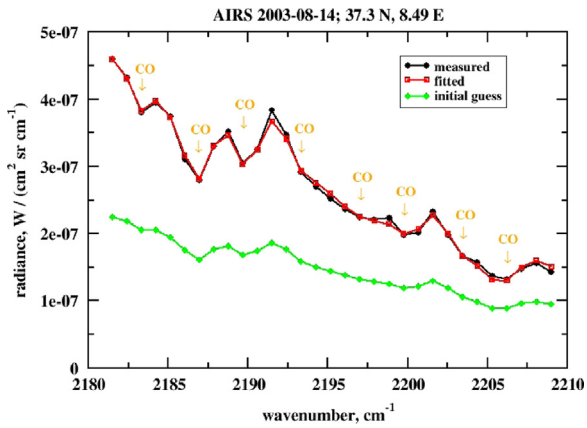

Fig. 12. Comparison of observed vs. modeled thermal infrared spectra for a nadir sounding geometry: AIRS observations over Portugal, August 2003.

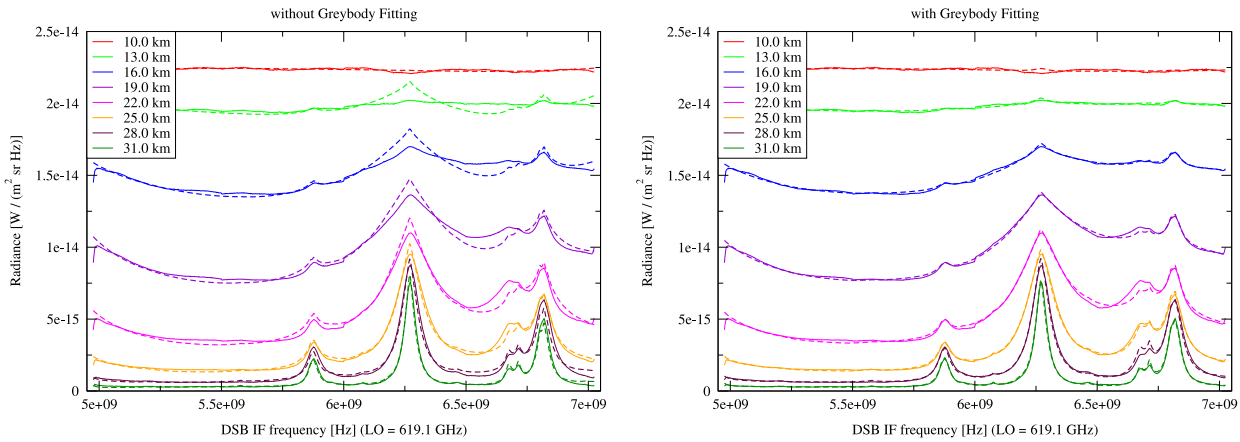

Fig. 11. TELIS submillimeter spectra observed during the January 2010 flight over Kiruna and compared with GARLIC synthetic spectra: (a) without greybody, (b) with greybody fitted. DSB stands for "double sideband", and IF is "intermediate frequency", see also Section 3.6 and Fig. 4.

upwelling thermal radiation. The retrieval program PyReS (Prototype Retrieval System) that performed these inversions uses MIRART modules as the forward model for nadir IR radiative transfer and PORT library routines [120,121] for minimizing the residuals. The atmosphere was modeled with midlatitude summer profiles of temperature, CO, H_2O, CH_4, CO_2 (with 370 ppm) and N_2O. Retrieval parameters were scaling factors for the temperature, CO and H_2O profiles and the surface temperature. All parameters were retrieved simultaneously in the spectral microwindow 2180–2210 cm^{-1}. The example result in Fig. 12 shows an AIRS spectrum with a pixel containing a forest fire region covering about 2.5% of the pixel area. This percentage was estimated from corresponding MODIS data with the help of the Dozier [124] method. The average pixel surface temperature retrieved was 327 K, where the relatively low value is explained by the small percentage of the fire area. The retrieved CO concentration was almost doubled compared to nearby undisturbed marine pixels. Analysis of the Jacobians showed that the top-of-atmosphere radiance is mainly affected by the CO concentration at 5 km altitude. The modeled spectrum (Fig. 12) shows very good agreement with the AIRS measurement in most spectral points. The largest relative deviation is 5.2% at 2209 cm^{-1}.

4.3.3. Beyond schwarzschild: MIPAS cloud spectra

While scattering is often neglected in infrared and microwave radiative transfer, it can be relevant in these spectral regions in the Earth atmosphere, e.g., in the occurrence of clouds [125,126]. Microwave and infrared limb sounders have been applied for measurements of upper tropospheric ice clouds [127–130], and sub-millimetre instruments have been successfully proposed for improved measurements of cloud ice mass [131], where all of these techniques are based on the scattering effects of clouds.

Scattering by ice clouds modifies the broadband continuum signal in the region of atmospheric windows. Interacting with line absorption, it furthermore causes broad absorption line structures in cloudy spectra that occur in place of narrow emission lines in clear-sky spectra. While the continuum signal might be approximated by grey-body extinction, the latter features can only be reproduced when scattering is explicitly modeled. This can help to improve the retrieval of temperature and trace gas profiles (e.g., [132]), but also allows for retrievals of cloud properties.

For handling cloudy spectra, the scattering model SARTre (Spherical Atmospheric Radiative Transfer) was developed as an extension of MIRART [133] replacing the Schwarzschild equation by a more complete formulation. The optical depth τ in Eq. (1b) is generalized to

$$\tau(\nu,s) = \int_0^s (\alpha(\nu,s') + \alpha_c(\nu,s') + \beta_c(\nu,s'))\, ds' \tag{23}$$

comprising absorption by gaseous components (α) as well as absorption and scattering by clouds (α_c and β_c, respectively). Furthermore, the source term J in Eq. (1b) is given by

$$\begin{aligned} J(\nu,\tau,\Omega) &= J_B(\nu,\tau) + J_{MS}(\nu,\tau,\Omega) \\ &= (1-\omega_0(\nu,\tau))\, B(\nu,T(\tau)) \\ &\quad + \omega_0(\nu,\tau) \int_0^{4\pi} P(\nu,\tau,\Omega'\cdot\Omega)\, I(\nu,\tau,\Omega')\, d\Omega', \end{aligned} \tag{24}$$

where J_B describes thermal emission and J_{MS} the (multiple) scattering source term with $\omega_0 = \beta_c/(\alpha+\alpha_c+\beta_c)$ being the

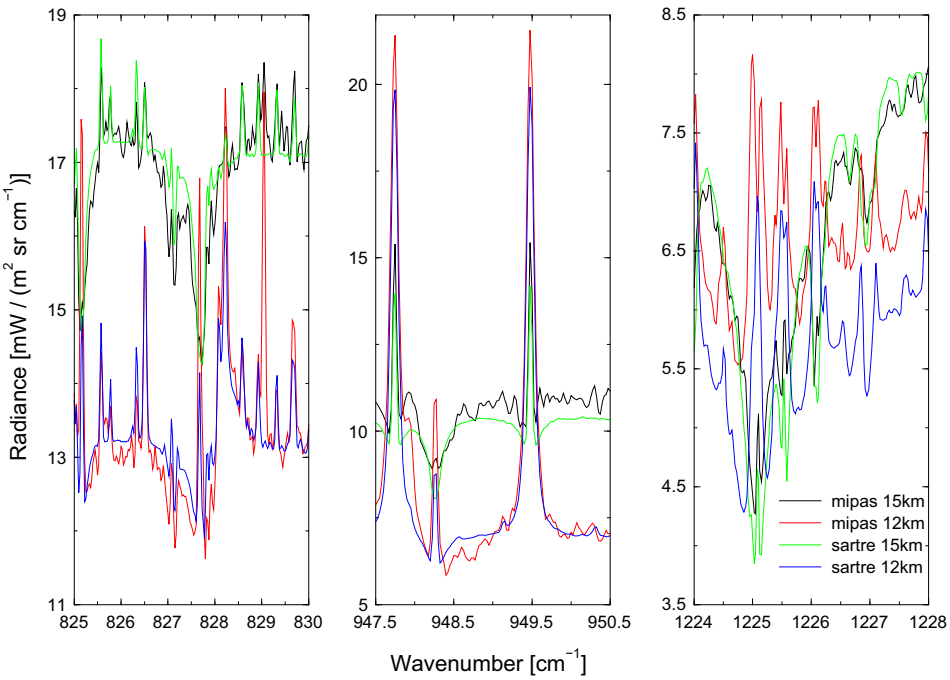

Fig. 13. Comparison of MIPAS observations (orbit 7203, July 17, 2003, limb sequence over the Arabian peninsula), and SARTRE simulations. Note that certain line features seen in the observations are absent in the simulations (an OCS line around 829 cm^{-1} and an SF_6 line around 948 cm^{-1}) as minor absorption species have been neglected in the simulations.

single scattering albedo and $P(\nu,\tau,\Omega'\cdot\Omega)$ the phase function characterizing the probability of scattering of radiation from direction Ω' into the line-of-sight direction Ω. Using a pseudo-spherical approach, the incident intensity $I(\nu,\tau,\Omega')$ is computed by DISORT [134] assuming a (locally) plane-parallel atmosphere at the intersections of the line-of-sight with the atmospheric levels.

Reproducing observed spectra of cloudy scenes requires proper modeling of both the gas as well as the cloud contributions. In Fig. 13, we compare modeled IR limb spectra to MIPAS [90] data classified as cloudy in order to validate (a) the implementation of the scattering module SARTre and its integration with the MIRART/GARLIC code in conjunction with (b) the modeling of molecular absorption. For the comparison, three microwindows between 8 and 12 μm were chosen each covering at least one H_2O line. Cloud properties were estimated comparing the continuum signals of observed and modeled limb spectra at two subsequent tangent altitudes. The best fit (see Fig. 13) was found for a cirrus with cloud top around 15.5 km, an ice water path of $\mathrm{IWP}=0.1\ \mathrm{g/m^2}$ and an effective particle size of $D_e=10\ \mu\mathrm{m}$. For these cloud properties, simulated and observed broadband signals are in close agreement in all three microwindows. Furthermore, finer structures observed in the MIPAS spectra like H_2O absorption signatures caused by scattering of radiation into the line-of-sight are reproduced well. Deviations between measurement and simulation (particularly in the right panel of Fig. 13) can largely be explained by deviations in the atmospheric profiles (e.g., water vapor and temperature) assumed in the simulations and by cloud inhomogeneities. Further details on the fitting procedure and a discussion of results are given in Mendrok [133] and Mendrok et al. [135].

4.3.4. Venus: transit spectroscopy and SCIAMACHY

Originally, MIRART was developed for radiative transfer modeling of Earth's atmosphere. In recent years, however, MIRART and GARLIC have been successfully used for radiative transfer analysis of planetary atmospheres. Currently MIRART/GARLIC is used for studies of the infrared signature of extra-solar planets, in particular for assessments of the feasibility to detect biosignatures (spectral features of molecules related to life) in emission or transmission spectra of Earth-like exoplanets (e.g., [117,136–139]).

During the transit of Venus in June 2004, transmission spectra of its upper atmosphere were observed in the near infrared with an echelle spectrograph of the Vacuum Tower Telescope (VTT) in Tenerife. Despite the suboptimal measurement conditions it was clearly possible to identify numerous CO_2 absorption lines (transmission values above one are mostly due to noise, the large feature at about 6258.25 $\mathrm{cm^{-1}}$ is related to the solar spectrum). Comparison of the observed spectra with synthetic spectra generated with MIRART allowed estimation of the relative abundance of the three most abundant CO_2 isotopologues [140], essentially confirming the literature values within the error margin. Fig. 14 shows a comparison of the "best-fit" model spectrum with the observed spectrum.

The original idea of targeting SCIAMACHY (Scanning Imaging Absorption Spectrometer for Atmospheric CHartographY [141]) to Venus has been to observe our neighbour planet as a perfect point source in order to improve the instrument's field-of-view characterization. However, the radiometric and spectral quality of the data was surprisingly good; in particular this offered the opportunity to validate the implementation of the single-scattering solver in GARLIC. This approach was used to model the radiative transfer in the thin upper haze layer above the dense, opaque main cloud deck approximated as a perfectly reflecting surface. In analogy to Eq. (24), a source function $J=J_B+J_{SS}$ is used with the single scattering source term described by

$$J_{SS}(\nu,\tau,\Omega)=\omega_0(\nu,\tau)\,P(\nu,\tau,\Omega_0\cdot\Omega)\,I_0(\nu,\Omega_0)\,\mathrm{e}^{-\tau_0(\nu)} \tag{25}$$

where I_0 is the solar radiation at top-of-atmosphere with incident direction Ω_0 and the transmission $\mathrm{e}^{-\tau_0}$ describes the attenuation of the solar beam along the path through the atmosphere to the scattering point. The haze particles were assumed to have a unimodal log-normal particle size distribution with mode diameter 0.3 μm and standard deviation 1.56 μm. Fig. 15 shows a comparison of measured SCIAMACHY channel 6 spectra with simulations, where a nadir or

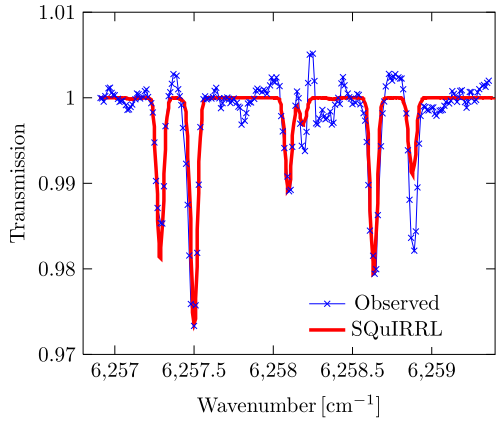

Fig. 14. Comparison of Venus near infrared observations and MIRART-SQuIRRL simulations: Venus transit spectrum observed by an echelle spectrograph at VTT, Tenerife (Spain).

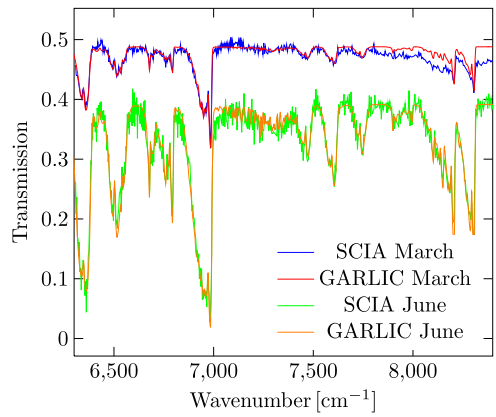

Fig. 15. Comparison of Venus near infrared observations and GARLIC simulations: Venus observed by SCIAMACHY aboard Envisat.

limb viewing geometry has been assumed for the March and June 2009 observations, respectively.

5. Conclusions

We have presented a new lbl code GARLIC providing a detailed discussion of algorithmic and computational aspects considered as novel and/or unique. A combination of two rational approximations for the complex error function and a multigrid algorithm constitute the core of the code. Subroutines of GARLIC serve as forward models for several retrieval codes, where the Jacobians are implemented using automatic differentiation thus providing exact derivatives in short time.

For the evaluation of the integrals along the line-of-sight in the Schwarzschild and Beer equations GARLIC utilizes various quadrature schemes. The performance of these schemes has been tested by comparison of top-of-atmosphere radiances in the 9.6 μm band of ozone, by intercomparisons of thermal emission limb spectra of GARLIC vs. KOPRA, and by intercomparisons of GARLIC with ARTS for down- and up-looking geometries in the microwave; the results indicate the superiority of the trapezoid-Laguerre quadrature scheme using optical depth as integration variable. Note that because the trapezoid quadrature is a local approximation (i.e. only a single interval or layer is evaluated), this approach is advantageous compared to quadratures based on overlapping parabola for situations featuring discontinuities of the optical properties, e.g., at cloud top or bottom.

Concerning applications to planetary science, both ground-based VTT and spaceborne SCIAMACHY observations of Venus were successfully modeled with GARLIC and demonstrate the capability to model atmospheric absorption and radiative transfer in atmospheres significantly different from Earth.

Outlook: So far the development of GARLIC was largely driven by applications. An upgrade of the water continuum with a recent version of the MT-CKD continuum [35] and implementation of the TIPS (Total Internal Partition Sum [119]) scheme modeling the temperature dependence of the line strengths is planned for the near future and might help to resolve some of the discrepancies found in code intercomparisons. New features to be implemented might include more sophisticated line shapes (e.g., Rautian and Galatry profiles for collisional narrowing [45], speed-dependent profiles [46,142], sub/super-Lorentzian line shapes) or line mixing to account for the improved quality of current and future sensors (e.g., [143–145]). A two-dimensional or three-dimensional description of the atmosphere would allow investigations of horizontal inhomogeneity effects in limb observations or tomographic retrieval approaches required for future space missions. And finally, data amount and data quality of future sensors will increase further, so exploration of algorithms and implementations esp. for the lbl modeling of cross sections will likely continue forever.

Acknowledgements

Thanks to Thomas von Clarmann, Gabriele Stiller, and Michael Höpfner at Karlsruhe Institute of Technology — Institute for Meteorology and Climate Research, and Stefan Bühler and Mathias Milz of the Division of Space Technology, Lulea University of Technology for numerous discussions. AMIL2DA was a Shared Cost Action within the RTD generic activities of the 5th FP EESD Programme of the European Commission, project EVG1-CT-1999-00015. Financial support by the Helmholtz Research Alliance "Planetary Evolution and Life" and within the ESA-ESTEC study "ESAS-Light" (Contract no. AO/1-5433/07/NL/HE) is greatly appreciated.

Appendix A. Cubic Hermite interpolation

The coefficients of the cubic polynomial:

$$p(x+\delta) = a_0 + a_1\delta + a_2\delta^2 + a_3\delta^3 \quad \text{for } 0 \le \delta \le x_\mathrm{r} - x_\mathrm{l} \equiv \Delta \tag{A.1}$$

interpolating $y(x)$ in the interval $x_\mathrm{l} \le x \le x_\mathrm{r}$ are determined by the continuity conditions for function values and first derivatives at the left and right interval bounds:

$$p(x_\mathrm{l}) = y(x_\mathrm{l}) \equiv y_\mathrm{l}, \quad p(x_\mathrm{r}) = y(x_\mathrm{r}) \equiv y_\mathrm{r} \tag{A.2}$$

$$p'(x_\mathrm{l}) = y'(x_\mathrm{l}) \equiv d_\mathrm{l}, \quad p'(x_\mathrm{r}) = y'(x_\mathrm{r}) \equiv d_\mathrm{r} \tag{A.3}$$

and are given by

$$a_0 = y_\mathrm{l} \tag{A.4}$$

$$a_1 = d_\mathrm{l} \tag{A.5}$$

$$a_2 = [3(y_\mathrm{r} - y_\mathrm{l}) - (d_\mathrm{r} + 2d_\mathrm{l})\Delta]/\Delta^2 \tag{A.6}$$

$$a_3 = [2(y_\mathrm{l} - y_\mathrm{r}) + (d_\mathrm{r} + d_\mathrm{l})\Delta]/\Delta^3. \tag{A.7}$$

For the midpoint one finds

$$p(x+\Delta/2) = p((x_\mathrm{r} + d_\mathrm{l})/2) = \frac{1}{2}(y_\mathrm{l} + y_\mathrm{l}) + \frac{\Delta}{8}(d_\mathrm{l} - d_\mathrm{r}). \tag{A.8}$$

Appendix B. Overlapping parabola quadrature

Although conceptually quite simple, the quadrature based on overlapping parabola is rarely treated in textbooks on numerical analysis [146]. Let $p_i(x) \equiv a_i x^2 + b_i x + c_i$ denote the quadratic polynomial that interpolates y at the triple of points $(x_{i-1}, y_{i-1}), (x_i, y_i)$, and (x_{i+1}, y_{i+1}) (for $1 \le i \le n-1$). To evaluate the integral of a function $y(x)$ given a finite set of data pairs $\{(x_0, y_0), (x_1, y_1), \ldots, (x_n, y_n)\}$, the integrand in each subinterval $[x_{i-1}, x_i]$ is approximated by the mean of the interpolating quadratic polynomials p_i and p_{i-1}:

$$\int_a^b f(x)\,\mathrm{d}x = \int_a^{x_1} p_1(x)\,\mathrm{d}x + \int_{x_{n-1}}^b p_{n-1}(x)\,\mathrm{d}x + \sum_{i=1}^{n-2} \int_{x_i}^{x_{i+1}} \frac{p_i(x) + p_{i+1}(x)}{2}\,\mathrm{d}x \tag{B.1}$$

for $x_0 \le a < x_1$ and $x_{n-1} < b \le x_n$. A Fortran 77 implementation of the overlapping parabola rule is provided by the SLATEC [147] subroutine `(D)AVINT`.

The relative simplicity of the overlapping parabola quadrature made an optimization straightforward, resulting in an accelerated algorithm only slightly slower than trapezoid quadrature. Some reorganization of the code

already resulted in considerable speed-up: moving IF statements outside a DO loop, avoiding unnecessary divisions, and skipping repeated checks of input parameters. Furthermore, calculation of the radiance (1) also requires knowledge of the transmission $\mathcal{T}(\nu, s')$ as a function of distance to the observer s', i.e. for all path grid points s_j between observer and end-of-path. In this case the weights w_j can be calculated once and the stepwise quadrature from a fixed starting point to a sequence of end points s_j can be formulated as a matrix–vector product.

Appendix C. Trapezoid-Laguerre quadrature

The trapezoidal rule is the most basic and important Newton–Cotes formula for numerical evaluation of an integral of a function $y(x)$:

$$\int_{x_0}^{x_n} y(x)\,\mathrm{d}x = \frac{1}{2}\sum_{i=1}^{n}(y_i + y_{i-1})(x_i - x_{i-1}). \tag{C.1}$$

Clearly the assumption behind the trapezoid rule, i.e. a linear polynomial interpolating the function y in the subintervals $[x_{i-1}, x_i]$, is hardly justified in the presence of the exponential factor in Eq. (1b). A generalization in analogy to Gauss quadrature rules with weight functions yields the Trapezoid-Laguerre quadrature for

$$\int_{x_0}^{x_n} y(x)\mathrm{e}^{-x}\,\mathrm{d}x \tag{C.2}$$

Assuming linear interpolation of $y(x) \approx a_i x + b_i$ with $b_i = y_{i-1} - a_i x_{i-1}$ in each subinterval, using $\int x\,\mathrm{e}^{-x}\,\mathrm{d}x = -\mathrm{e}^{-x}(1+x)$, and rearranging terms to avoid cancellation errors finally gives

$$\int_{x_0}^{x_n} y(x)\mathrm{e}^{-x}\,\mathrm{d}x$$

$$= y_0\mathrm{e}^{-x_0} - y_n\mathrm{e}^{-x_n} + \sum_{i=1}^{n}(y_i - y_{i-1})\mathcal{E}(x_i - x_{i-1})\mathrm{e}^{-x_{i-1}}, \tag{C.3}$$

where $\mathcal{E}(\Delta x) \equiv (1 - \mathrm{e}^{-\Delta x})/\Delta x$ denotes the relative exponential function. Because the quadrature nodes are monotone increasing, $x_i \geq x_{i-1}$, the relative error function can be computed in a robust way even for small arguments by exploiting the Taylor expansion $\mathcal{E}(-t) \approx \sum_{j=0}^{\infty}(-t)^j/(j+1)!$.

Appendix D. *B* exponential in optical depth approximation

To simplify the notation use $B(\tau) \equiv B(T(\tau))$. The Planck function within a layer $\tau_{l-1} \leq \tau < \tau_l$ is approximated by

$$B(\tau) = B(\tau_{l-1})\mathrm{e}^{-\beta_l(\tau - \tau_{l-1})} \quad \text{with } \beta_l = \frac{\ln(B(\tau_{l-1})/B(\tau_l))}{\tau_l - \tau_{l-1}}. \tag{D.1}$$

Using this approximation in the Schwarzschild integral (1b) (with $\tau_0 = 0$, $\tau_\mathrm{b} \equiv \tau_L$ and the background term ignored) gives

$$\begin{aligned} I(\nu) &= \int_0^{\tau_L} B(\tau)\mathrm{e}^{-\tau}\,\mathrm{d}\tau \\ &= \sum_{l=1}^{L}\int_{\tau_{l-1}}^{\tau_l} B(\tau)\mathrm{e}^{-\tau}\,\mathrm{d}\tau \\ &= \sum_{l=1}^{L} B(\tau_{l-1})\int_{\tau_{l-1}}^{\tau_l} \mathrm{e}^{-\beta_l(\tau-\tau_l)-\tau}\,\mathrm{d}\tau \end{aligned}$$

and finally

$$I(\nu) = \sum_{l=1}^{L}\frac{B(\tau_{l-1})}{\beta_l + 1}\left(\mathrm{e}^{-\tau_{l-1}} - \mathrm{e}^{-\beta_l(\tau_l - \tau_{l-1}) - \tau_l}\right) \tag{D.2}$$

Note that in case of identical optical depths at the layer boundaries, i.e. $\tau_{l-1} = \tau_l$, the current layer is combined with the next layer.

References

[1] Goody RM, Yung YL. Atmospheric radiation—theoretical basis. 2nd ed.. Oxford University Press; 1989.

[2] Liou Kuo-Nan. An introduction to atmospheric radiation. 2nd ed.. Academic Press; 2002.

[3] Zdunkowski W, Trautmann T, Bott A. Radiation in the atmosphere—a course in theoretical meteorology. Cambridge University Press; 2007.

[4] Carli B, Ade P, Carlotti M, Cortesi U, Gignoli A, Hamilton P, et al. Minor constituent concentrations measured from a high altitude aircraft using high resolution far-infrared Fourier transform spectroscopy. J Atmos Chem 2000;35:273–93. http://dx.doi.org/10.1023/A:1006316026239.

[5] Dinelli BM, Castelli E, Carli B, Del Bianco S, Gai M, Santurri L, et al. Technical note: measurement of the tropical UTLS composition in presence of clouds using millimetre-wave heterodyne spectroscopy. Atmos Chem Phys 2009;9(4):1191–207. http://dx.doi.org/10.5194/acp-9-1191-2009.

[6] Woiwode W, Oelhaf H, Gulde T, Piesch C, Maucher G, Ebersoldt A, et al. MIPAS-STR measurements in the arctic UTLS in winter/spring 2010: instrument characterization, retrieval and validation. Atmos Meas Tech 2012;5(6):1205–28. http://dx.doi.org/10.5194/amt-5-1205-2012.

[7] Friedl-Vallon F, Maucher G, Seefeldner M, Trieschmann O, Kleinert A, Lengel A, et al. Design and characterization of the balloon-borne Michelson Interferometer for Passive Atmospheric Sounding (MIPAS-B2). Appl Opt 2004;43(16):3335–55. http://dx.doi.org/10.1364/AO.43.003335.

[8] Irimajiri Y, Manabe T, Ochiai S, Masuko H, Yamagami T, Saito Y, et al. BSMILES—a balloon-borne superconducting submillimeter-wave limb-emission sounder for stratospheric measurements. Geosci Remote Sens Lett 2006;3(1):88–92. http://dx.doi.org/10.1109/LGRS.2005.856712.

[9] Berk A, Anderson GP, Acharya PK, Bernstein LS, Muratov L, Lee J, et al. Modtran 5: a reformulated atmospheric band model with auxiliary species and practical multiple scattering options: update. In: Shen SS, Lewis PE, editors. Algorithms and technologies for multispectral, hyperspectral, and ultraspectral imagery XI, vol. 5806. SPIE; 2005. p. 662–7. http://dx.doi.org/10.1117/12.606026.

[10] Lacis AA, Oinas V. A description of the correlated *k* distribution method for modeling nongray gaseous absorption, thermal emission, and multiple scattering in vertically inhomogeneous atmospheres. J Geophys Res 1991;96:9027–63. http://dx.doi.org/10.1029/90JD01945.

[11] Wiscombe WJ, Evans JW. Exponential-sum fitting of radiative transmission functions. J Comput Phys 1977;24:416–44. http://dx.doi.org/10.1016/0021-9991(77)90031-6.

[12] Gordley LL, Russell III JM. Rapid inversion of limb radiance data using an emissivity growth approximation. Appl Opt 1981;20:807–13. http://dx.doi.org/10.1364/AO.20.000807.

[13] Bernstein LS, Berk A, Sundberg RL. Application of MODTRAN to extra-terrestrial planetary atmospheres. Technical report, Spectral Sciences, Inc., Burlington, MA, 2007. URL: ⟨http://www.amostech.com/TechnicalPapers/2007/Astronomy/Bernstein.pdf⟩.

[14] Mischna MA, Lee C, Richardson M. Development of a fast, accurate radiative transfer model for the Martian atmosphere, past and present. J Geophys Res 2012;117(E10). http://dx.doi.org/10.1029/2012JE004110.
[15] Sromovsky LA, Fry PM, Boudon V, Campargue A, Nikitin A. Comparison of line-by-line and band models of near-IR methane absorption applied to outer planet atmospheres. Icarus 2012;218(1):1–23. http://dx.doi.org/10.1016/j.icarus.2011.12.008.
[16] Carli B, Aubertin G, Birk M, Carlotti M, Castelli E, Ceccherini S, et al. The global picture of the atmospheric composition provided by MIPAS on Envisat. In: IEEE international geoscience and remote sensing symposium (IGARSS), 2012. p. 1860–3 http://dx.doi.org/10.1109/IGARSS.2012.6351144.
[17] Kraft S, Caron J, Bezy J-L, Meynart R, Langen J, Dominguez BC, et al. PREMIER's imaging IR limb sounder. In: Proceedings of SPIE, sensors, systems, and next-generation satellites XV, vol. 8176A, 2011. http://dx.doi.org/10.1117/12.898328.
[18] Rothman LS, Gordon IE, Babikov Y, Barbe A, Chris Benner D, Bernath PF, et al. The HITRAN2012 molecular spectroscopic database. J Quant Spectrosc Radiat Transfer 2013;130:4–50. http://dx.doi.org/10.1016/j.jqsrt.2013.07.002.
[19] Rothman LS, Gordon IE, Barber RJ, Dothe H, Gamache RR, Goldman A, et al. HITEMP, the high-temperature molecular spectroscopic database. J Quant Spectrosc Radiat Transfer 2010;111(12–13):2139–50. http://dx.doi.org/10.1016/j.jqsrt.2010.05.001.
[20] Tennyson J, Yurchenko SN. ExoMol: molecular line lists for exoplanet and other atmospheres. Mon Not R Astron Soc 2012;425(1):21–33. http://dx.doi.org/10.1111/j.1365-2966.2012.21440.x.
[21] Clough SA, Kneizys FX, Rothman LS, Gallery WO. Atmospheric transmittance and radiance: FASCOD1B. Proc SPIE 1981;277:152–66.
[22] Scott NA, Chédin. A fast line-by-line method for atmospheric absorption computations: the automatized atmospheric absorption Atlas. J Appl Meteorol 1981;20(7):802–12. http://dx.doi.org/10.1175/1520-0450 (1981)020(0802:AFLBLM)2.0.CO;2.
[23] Edwards DP. Atmospheric transmittance and radiance calculations using line-by-line computer models. In: Modelling of the atmosphere, Proceedings of SPIE, vol. 928, 1988. p. 94–116.
[24] Clough SA, Shephard MW, Mlawer EJ, Delamere JS, Iacono MJ, Cady-Pereira K, et al. Atmospheric radiative transfer modeling: a summary of the AER codes. J Quant Spectrosc Radiat Transfer 2005;91(2):233–44. http://dx.doi.org/10.1016/j.jqsrt.2004.05.058.
[25] Bühler SA, Eriksson P, Kuhn T, von Engeln A, Verdes C, ARTS. the atmospheric radiative transfer simulator. J Quant Spectrosc Radiat Transfer 2005;91:65–93. http://dx.doi.org/10.1016/j.jqsrt.2004.05.051.
[26] Eriksson P, Buehler SA, Davis S, Emde C, Lemke O. ARTS, the atmospheric radiative transfer simulator, version 2. J Quant Spectrosc Radiat Transfer 2011;112(10):1551–8. http://dx.doi.org/10.1016/j.jqsrt.2011.03.001.
[27] Schreier F, Schimpf B. A new efficient line-by-line code for high resolution atmospheric radiation computations incl. derivatives. In: Smith WL, Timofeyev Y, editors. IRS 2000: current problems in atmospheric radiation. A. Deepak Publishing; 2001. p. 381–4.
[28] Schreier F, Böttger U. MIRART, a line-by-line code for infrared atmospheric radiation computations incl. derivatives. Atmos Ocean Opt 2003;16:262–8.
[29] von Clarmann T, Höpfner M, Funke B, López-Puertas M, Dudhia A, Jay V, et al. Modeling of atmospheric mid-infrared radiative transfer: the AMIL2DA algorithm intercomparison experiment. J Quant Spectrosc Radiat Transfer 2002;78:381–407, http://dx.doi.org/10.1016/S0022-4073(02)00262-5.
[30] Melsheimer C, Verdes C, Bühler SA, Emde C, Eriksson P, Feist DG, et al. Intercomparison of general purpose clear sky atmospheric radiative transfer models for the millimeter/submillimeter spectral range. Radio Sci 2005;40:RS1007. http://dx.doi.org/10.1029/2004RS003110.
[31] Armstrong BH. Spectrum line profiles: the Voigt function. J Quant Spectrosc Radiat Transfer 1967;7:61–88. http://dx.doi.org/10.1016/0022-4073(67)90057-X.
[32] Jacquinet-Husson N, Scott NA, Chedin A, Crepeau L, Armante R, Capelle V, et al. The GEISA spectroscopic database: current and future archive for Earth and planetary atmosphere studies. J Quant Spectrosc Radiat Transfer 2008;109:1043–59. http://dx.doi.org/10.1016/j.jqsrt.2007.12.015.
[33] Jacquinet-Husson N, Scott NA, Chédin A, Garceran K, Armante R, Chursin AA, et al. The 2003 edition of the GEISA/IASI spectroscopic database. J Quant Spectrosc Radiat Transfer 2005;62:205–54. http://dx.doi.org/10.1016/j.jqsrt.2004.12.004.
[34] Clough SA, Kneizys FX, Davies R. Line shape and the water vapor continuum. Atmos Res 1989;23:229–41. http://dx.doi.org/10.1016/0169-8095(89)90020-3.
[35] Mlawer EJ, Payne VH, Moncet J-L, Delamere JS, Alvarado MJ, Tobin DC. Development and recent evaluation of the MT-CKD model of continuum absorption. Philos Trans R Soc A: Math Phys Eng Sci 2012;370(1968):2520–56. http://dx.doi.org/10.1098/rsta.2011.0295.
[36] Richard C, Gordon IE, Rothman LS, Abel M, Frommhold L, Gustafsson M, et al. New section of the HITRAN database: collision-induced absorption (CIA). J Quant Spectrosc Radiat Transfer 2012;113(11):1276–85. http://dx.doi.org/10.1016/j.jqsrt.2011.11.004.
[37] Olivero JJ, Longbothum RL. Empirical fits to the Voigt line width: a brief review. J Quant Spectrosc Radiat Transfer 1977;17:233–6. http://dx.doi.org/10.1016/0022-4073(77)90161-3.
[38] Abramowitz M, Stegun IA. Handbook of mathematical functions. New York: National Bureau of Standards, AMS55; 1964.
[39] Olver Frank WJ, Lozier Daniel W, Boisvert Ronald F, Clark Charles W, editors. NIST handbook of mathematical functions. Cambridge University Press; 2010.
[40] Twitty JT, Rarig PL, Thompson RE. A comparison of fast codes for the evaluation of the Voigt profile function. J Quant Spectrosc Radiat Transfer 1980;24:529–32. http://dx.doi.org/10.1016/0022-4073(80)90022-9.
[41] Klim A. A comparison of methods for the calculation of Voigt profiles. J Quant Spectrosc Radiat Transfer 1981;26:537–45, http://dx.doi.org/10.1016/0022-4073(81)90041-8.
[42] Afonin SV, Gaponov VA, Gandrin AG. Comparative analysis of three procedures for calculation of the Voigt profile of a spectral line. J Appl Spectrosc 1984;41:868.
[43] Schreier F. The Voigt and complex error function: a comparison of computational methods. J Quant Spectrosc Radiat Transfer 1992;48:743–62. http://dx.doi.org/10.1016/0022-4073(92)90139-U.
[44] Thompson WJ. Numerous neat algorithms for the Voigt profile function. Comput Phys 1993;7:627. http://dx.doi.org/10.1063/1.4823236.
[45] Varghese PL, Hanson RK. Collisional narrowing effects on spectral line shapes measured at high resolution. Appl Opt 1984;23(14):2376–85. http://dx.doi.org/10.1364/AO.23.002376.
[46] Tran H, Ngo NH, Hartmann J-M. Efficient computation of some speed-dependent isolated line profiles. J Quant Spectrosc Radiat Transfer 2013;129:199–203 ⟨http://dx.doi.org/10.1016/j.jqsrt.2013.06.015⟩.
[47] Hui AK, Armstrong BH, Wray AA. Rapid computation of the Voigt and complex error functions. J Quant Spectrosc Radiat Transfer 1978;19:509–16. http://dx.doi.org/10.1016/0022-4073(78)90019-5.
[48] Humliček J. An efficient method for evaluation of the complex probability function: the Voigt function and its derivatives. J Quant Spectrosc Radiat Transfer 1979;21:309–13. http://dx.doi.org/10.1016/0022-4073(79)90062-1.
[49] Humliček J. Optimized computation of the Voigt and complex probability function. J Quant Spectrosc Radiat Transfer 1982;27:437–44. http://dx.doi.org/10.1016/0022-4073(82)90078-4.
[50] Kochanov VP. Efficient approximations of the Voigt and Rautian–Sobelman profiles. Atmos Ocean Opt 2011;24(5):432–5, http://dx.doi.org/10.1134/S1024856011050071.
[51] Weideman JAC. Computation of the complex error function. SIAM J Numer Anal 1994;31:1497–518. http://dx.doi.org/10.1137/0731077.
[52] Schreier F. Optimized implementations of rational approximations for the Voigt and complex error function. J Quant Spectrosc Radiat Transfer 2011;112(6):1010–25. http://dx.doi.org/10.1016/j.jqsrt.2010.12.010.
[53] Kuntz M. A new implementation of the Humlicek algorithm for the calculation of the Voigt profile function. J Quant Spectrosc Radiat Transfer 1997;57:819–24. http://dx.doi.org/10.1016/S0022-4073(96)00162-8.
[54] Imai K, Suzuki M, Takahashi C. Evaluation of Voigt algorithms for the ISS/JEM/SMILES L2 data processing system. Adv Space Res 2010;45:669–75. http://dx.doi.org/10.1016/j.asr.2009.11.005.
[55] Stiller GP, von Clarmann T, Funke B, Glatthor N, Hase F, Höpfner M, et al. Sensitivity of trace gas abundances retrievals from infrared limb emission spectra to simplifying approximations in radiative transfer modelling. J Quant Spectrosc Radiat Transfer 2002;72:249–80. http://dx.doi.org/10.1016/S0022-4073(01)00123-6.
[56] Urban J, Lautié N, Le Flochmoën E, Jiménez C, Eriksson P, Dupuy E, et al. Odin/SMR limb observations of stratospheric trace gases: level 2 processing of ClO, N_2O, O_3, and HNO_3. J Geophys Res 2005;110. http://dx.doi.org/10.1029/2004JD005741.
[57] Kohlert D, Schreier F. Line-by-line computation of atmospheric infrared spectra with field programmable gate arrays. IEEE J Sel Top

Earth Obs Remote Sens 2011;4(3):701–9. http://dx.doi.org/10.1109/JSTARS.2010.2098395.
[58] Clough SA, Kneizys FX. Convolution algorithm for the Lorentz function. Appl Opt 1979;18:2329–33. http://dx.doi.org/10.1364/AO.18.002329.
[59] West R, Crisp D, Chen L. Mapping transformations for broadband atmospheric radiation calculations. J Quant Spectrosc Radiat Transfer 1990;43(3):191–9. http://dx.doi.org/10.1016/0022-4073(90)90051-7.
[60] Gordley LJ, Marshall BT, Chu DA. LINEPAK: algorithms for modeling spectral transmittance and radiance. J Quant Spectrosc Radiat Transfer 1994;52:563. http://dx.doi.org/10.1016/0022-4073(94)90025-6.
[61] Fomin BA. Effective interpolation technique for line-by-line calculation of radiation absorption in gases. J Quant Spectrosc Radiat Transfer 1995;53:663–9. http://dx.doi.org/10.1016/0022-4073(95)00029-K.
[62] Sparks L. Efficient line-by-line calculation of absorption coefficients to high numerical accuracy. J Quant Spectrosc Radiat Transfer 1997;57:631–50. http://dx.doi.org/10.1016/S0022-4073(96)00154-9.
[63] Titov DV, Haus R. A fast and accurate method of calculation of gaseous transmission functions in planetary atmospheres. Planet Space Sci 1997;45:369–77. http://dx.doi.org/10.1016/S0032-0633(96)00129-8.
[64] Kuntz M, Höpfner M. Efficient line-by-line calculation of absorption coefficients. J Quant Spectrosc Radiat Transfer 1999;63:97–114. http://dx.doi.org/10.1016/S0022-4073(98)00140-X.
[65] Kruglanski M, De Mazière M. Fast method for calculating infrared spectral transmittances in the wings of absorption lines. J Quant Spectrosc Radiat Transfer 2005;94:117–25. http://dx.doi.org/10.1016/j.jqsrt.2004.09.001.
[66] Schreier F. Optimized evaluation of a large sum of functions using a three-grid approach. Comput Phys Commun 2006;174:783–802. http://dx.doi.org/10.1016/j.cpc.2005.12.015.
[67] Kahaner D, Moler C, Nash S. Numerical methods and software. Englewood Cliffs, NJ: Prentice-Hall; 1989.
[68] Dahlquist G, Björck Å. Numerical methods in scientific computing, vol. 1. SIAM; 2008.
[69] Kindratenko V. Novel computing architectures. Comput Sci Eng 2009;11(3):54–7. http://dx.doi.org/10.1109/MCSE.2009.56.
[70] Collange S, Daumas M, Defour D. Line-by-line spectroscopic simulations on graphics processing units. Comput Phys Commun 2008;178(2):135–43. http://dx.doi.org/10.1016/j.cpc.2007.08.013.
[71] Clerbaux C, Boynard A, Clarisse L, George M, Hadji-Lazaro J, Herbin H, et al. Monitoring of atmospheric composition using the thermal infrared IASI/MetOp sounder. Atmos Chem Phys 2009;9(16):6041–54. http://dx.doi.org/10.5194/acp-9-6041-2009.
[72] Norton RH, Rinsland CP. ATMOS data processing and science analysis methods. Appl Opt 1991;30:389–400. http://dx.doi.org/10.1364/AO.30.000389.
[73] Pugh LA, Rao KN. Intensities from infrared spectra. In: Rao KN, editor. Molecular Spectroscopy: Modern Research, vol. II. Academic Press; 1976. p. 165–227.
[74] Smith MAH, Rinsland CP, Fridovich B, Rao KN. Intensities and collision broadening parameters from infrared spectra. In: Rao KN, editor. Molecular Spectroscopy: Modern Research, vol. III. Academic Press; 1985. p. 111–248.
[75] Anderson GP, Clough SA, Kneizys FX, Chetwynd JH, Shettle EP. AFGL atmospheric constituent profiles (0–120 km). Technical report TR-86-0110, AFGL, 1986.
[76] Clough SA, Kneizys FX, Anderson GP, Shettle EP, Chetwynd JH, Abreu LW, et al. FASCOD3 spectral simulation. In: Lenoble J, Geleyn JF, editors. IRS'88: current problems in atmospheric radiation. A. Deepak Publishing; 1988. p. 372–5.
[77] Davis PhJ, Rabinowitz Ph. Numerical integration. Blaisdell Publishing Company; 1967.
[78] Rathke C, Fischer J. Evaluation of four approximate methods for calculating infrared radiances in cloudy atmospheres. J Quant Spectrosc Radiat Transfer 2002;75(3):297–321. http://dx.doi.org/10.1016/S0022-4073(02)00012-2.
[79] Gill PE, Murray W, Wright MH. Practical optimization.London, UK: Academic Press; 1981.
[80] Hurtmans D, Coheur P-F, Wespes C, Clarisse L, Scharf O, Clerbaux C, et al. FORLI radiative transfer and retrieval code for IASI. J Quant Spectrosc Radiat Transfer 2012;113(11):1391–408. http://dx.doi.org/10.1016/j.jqsrt.2012.02.036.
[81] Urban J, Baron P, Lautié N, Schneider N, Dassas K, Ricaud P, et al. Moliere (v5): a versatile forward- and inversion model for the millimeter and sub-millimeter wavelength range. J Quant Spectrosc Radiat Transfer 2004;83:529–54. http://dx.doi.org/10.1016/S0022-4073(03)00104-3.
[82] Amato U, Masiello G, Serio C, Viggiano M. The σ-IASI code for the calculation of infrared atmospheric radiance and its derivatives. Environ Model Softw 2002;17:651–67. http://dx.doi.org/10.1016/S1364-8152(02)00027-0. (Erratum: vol. 18, p. 97, 2003).
[83] Griewank A. Evaluating derivatives: principles and techniques of algorithmic differentiation. Philadelphia, PA: SIAM; 2000.
[84] Nocedal J, Wright S. Numerical optimization. Springer series in operations research and financial engineering. Springer; 2006.
[85] Bischof C, Carle A, Hovland P, Khademi P, Mauer A. ADIFOR 2.0 user's guide (revision D). Technical report ANL/MCS-TM-192, Argonne National Laboratory—Mathematics and Computer Science Division, 1998.
[86] Gimeno García S, Schreier F, Lichtenberg G, Slijkhuis S. Near infrared nadir retrieval of vertical column densities: methodology and application to SCIAMACHY. Atmos Meas Tech 2011;4(12):2633–57. http://dx.doi.org/10.5194/amt-4-2633-2011.
[87] Xu J, Schreier F, Vogt P, Doicu A, Trautmann T. A sensitivity study for far infrared balloon-borne limb emission sounding of stratospheric trace gases. Geosci Instrum Method Data Syst Disc 2013;3:251–303. http://dx.doi.org/10.5194/gid-3-251-2013.
[88] Hascoët L, Pascual V. The Tapenade automatic differentiation tool: principles, model, and specification. ACM Trans Math Softw 2013;39(3). http://dx.doi.org/10.1145/2450153.2450158.
[89] Bischof CH, Bücker HM. Computing derivatives of computer programs. In: Grotendorst J, editor. Modern methods and algorithms of quantum Chemistry: Proceedings. NIC Series, 2nd ed.. Jülich: John von Neumann Institute for Computing; 2000. p. 315–27.
[90] Fischer H, Birk M, Blom C, Carli B, Carlotti M, von Clarmann T, et al. MIPAS: an instrument for atmospheric and climate research. Atmos Chem Phys 2008;8(8):2151–88. http://dx.doi.org/10.5194/acp-8-2151-2008.
[91] Hase F, Hannigan JW, Coffey MT, Goldman A, Höpfner M, Jones NB, et al. Intercomparison of retrieval codes used for the analysis of high-resolution, ground-based FTIR measurements. J Quant Spectrosc Radiat Transfer 2004;87(1):25–52. http://dx.doi.org/10.1016/j.jqsrt.2003.12.008.
[92] Chance K, Kurucz RL. An improved high-resolution solar reference spectrum for Earth's atmosphere measurements in the ultraviolet, visible, and near infrared. J Quant Spectrosc Radiat Transfer 2010;111(9):1289–95. http://dx.doi.org/10.1016/j.jqsrt.2010.01.036.
[93] Pickett HM, Poynter RL, Cohen EA, Delitsky ML, Pearson JC, Müller HSP. Submillimeter, millimeter, and microwave spectral line catalog. J Quant Spectrosc Radiat Transfer 1998;60:883–90. http://dx.doi.org/10.1016/S0022-4073(98)00091-0.
[94] Echle G. Study of the retrieval of atmospheric trace gas profiles from infrared spectra. Draft report on task 1: continuum, ESA Contract 12055/96/NL/CN, 1997.
[95] Borysow A. Collision-induced absorption in the infrared: a data base for modelling planetry and stellar atmospheres. URL: ⟨http://www.astro.ku.dk/aborysow/programs/index.html⟩; 2002.
[96] Wordsworth R, Forget F, Eymet V. Infrared collision-induced and far-line absorption in dense CO_2 atmospheres. Icarus 2010;210(2):992–7. http://dx.doi.org/10.1016/j.icarus.2010.06.010.
[97] Johns JWC, Schreier F, Schimpf B, Birk M. Analysis of high-resolution Fourier transform molecular spectra. In: The future of spectroscopy: from astrophysics to biology. Quebec, CA: Sainte-Adéle; 1994.
[98] Badaoui M, Schreier F, Wagner Georg, Birk Manfred. Retrieval of line parameters from high resolution Fourier transform laboratory spectra in support of atmospheric spectroscopy. Phys Chem News 2007;36:1–9.
[99] Wagner G, Birk M, Schreier F, Flaud J-M. Spectroscopic database for ozone in the fundamental spectral regions. J Geophys Res 2002;107(D22):4626. http://dx.doi.org/10.1029/2001JD000818.
[100] Trucano T, Post D. Guest editors' introduction: verification and validation in computational science and engineering. Comput Sci Eng 2004;6(5):8–9. http://dx.doi.org/10.1109/MCSE.2004.38.
[101] Post Douglass E, Votta Lawrence G. Computational science demands a new paradigm. Physics Today 2005;58(1):35–41. http://dx.doi.org/10.1063/1.1881898.
[102] Boisvert RF, Cools R, Einarsson B. Assessment of accuracy and reliability. In: Einarsson Bo, editor. Accuracy and reliability in scientific computing. Philadelphia, PA: SIAM; 2005 [chapter 2].
[103] Fischer H, Anderson GP, von Clarmann Thomas, Clough SA, Coffey MT, Goldman A, et al., Intercomparison of transmittance and radiance algorithms (ITRA), Report of the Limb-Group of the ITRA Workshop at the University of Maryland, March 1986. KfK-Report 4349, Kernforschungszentrum Karlsruhe, FRG, 1988.

[104] Ellingson RG, Fouquart Y. The intercomparison of radiation codes in climate models: an overview. J Geophys Res 1991;96: 8925. http://dx.doi.org/10.1029/90JD01450.
[105] Soden B, Tjemkes S, Schmetz J, Saunders R, Bates J, Ellingson B, et al. An intercomparison of radiation codes for retrieving upper-tropospheric humidity in the 63-mm band: a report from the first GVaP workshop. Bull Am Meteorol Soc 2000;81(4):797–808.
[106] Garand L, Turner DS, Larocque M, Bates J, Boukabara S, Brunel P, et al. Radiance and Jacobian intercomparison of radiative transfer models applied to HIRS and AMSU channels. J Geophys Res 2001;106(D20): 24017–31. http://dx.doi.org/10.1029/2000JD000184.
[107] Tjemkes SA, Patterson T, Rizzi R, Shephard MW, Clough SA, Matricardi M, et al. The ISSWG line-by-line inter-comparison experiment. J Quant Spectrosc Radiat Transfer 2003;77(4): 433–53. http://dx.doi.org/10.1016/S0022-4073(02)00174-7.
[108] Kratz DP, Mlynczak MG, Mertens CJ, Brindley H, Gordley LL, Martin-Torres J, et al. An inter-comparison of far-infrared line-by-line radiative transfer models. J Quant Spectrosc Radiat Transfer 2005;90: 323–41. http://dx.doi.org/10.1016/j.jqsrt.2004.04.006.
[109] Strow LL, Hannon SE, De-Souza Machado S, Motteler HE, Tobin DC. Validation of the Atmospheric Infrared Sounder radiative transfer algorithm. J Geophys Res 2006;111:D09S06. http://dx.doi.org/10.1029/2005JD006146.
[110] Masiello G, Serio C, Esposito F, Palchetti L. Validation of line and continuum spectroscopic parameters with measurements of atmospheric emitted spectral radiance from far to mid infrared wave number range. J Quant Spectrosc Radiat Transfer 2012;113(11): 1286–99. http://dx.doi.org/10.1016/j.jqsrt.2012.01.019.
[111] Newman SM, Larar AM, Smith WL, Ptashnik IV, Jones RL, Mead MI. The joint airborne IASI validation experiment: an evaluation of instrument and algorithms. J Quant Spectrosc Radiat Transfer 2012;113(11):1372–90. http://dx.doi.org/10.1016/j.jqsrt.2012.02.030.
[112] Buehler SA, Kuvatov M, John VO, Leiterer U, Dier H. Comparison of microwave satellite humidity data and radiosonde profiles: a case study. J Geophys Res 2004;109(D13). http://dx.doi.org/10.1029/2004JD004605 ISSN 2156-2202.
[113] Chahine MT, Pagano TS, Aumann HH, Atlas R, Barnet C, Blaisdell J, et al. AIRS: improving weather forecasting and providing new data on greenhouse gases. Bull Am Meteorol Soc 2006;87: 911–26. http://dx.doi.org/10.1175/BAMS-87-7-911.
[114] Tobin DC, Revercomb HE, Taylor JK, Knuteson RO, DeSlover DH, Borg LA. Cross-track infrared sounder (CrIS) spectral radiance calibration and evaluations. In: Cahalan Robert F, Fischer Jürgen, editors. Radiation processes in the atmosphere and ocean (IRS2012): proceedings of the international radiation Symposium (IRC/IAMAS), AIP conference proceedings, vol. 1531, 2013. p. 724–7. http://dx.doi.org/10.1063/1.4804872.
[115] Beer R. TES on the Aura mission: scientific objectives, measurements, and analysis overview. IEEE Trans Geosci Remote Sens 2006;44:1102–5. http://dx.doi.org/10.1109/TGRS.2005.863716.
[116] Wiacek A, Strong K. Effects of vertical grid discretization in infrared transmission modeling. J Quant Spectrosc Radiat Transfer 2008;109:2463–90. http://dx.doi.org/10.1016/j.jqsrt.2008.03.015.
[117] Vasquez M, Schreier F, Gimeno García S, Kitzmann D, Patzer B, Rauer H, et al. Infrared radiative transfer in atmospheres of Earth-like planets around F, G, K, and M stars. I Clear-sky thermal emission spectra and weighting functions. A&A 2013;549: A26. http://dx.doi.org/10.1051/0004-6361/201219898.
[118] Schreier F, Gimeno García S, Milz M, Kottayil A, Höpfner M, von Clarmann T, et al., Intercomparison of three microwave/infrared high resolution line-by-line radiative transfer codes. In: Cahalan Robert F, Fischer Jürgen, editors. Radiation processes in the atmosphere and ocean (IRS2012): proceedings of the international radiation symposium (IRC/IAMAS), AIP conference proceedings, vol. 1531, 2013. p. 119–22. http://dx.doi.org/10.1063/1.4804722.
[119] Fischer J, Gamache RR, Goldman A, Rothman LS, Perrin A. Total internal partition sums for molecular species in the 2000 edition of the HITRAN database. J Quant Spectrosc Radiat Transfer 2003;82: 401–12. http://dx.doi.org/10.1016/S0022-4073(03)00166-3.
[120] Fox PA, Hall AD, Schryer NL. The PORT mathematical subroutine library. ACM Trans Math Softw 1978;4(June (2)):104–26, http://dx.doi.org/10.1145/355780.355789.
[121] Dennis Jr JE, Gay DM, Welsch RE. An adaptive nonlinear least-squares algorithm. ACM Trans Math Softw 1981;7(3):348–68, http://dx.doi.org/10.1145/355958.355965.
[122] von Clarmann T, Ceccherini S, Doicu A, Dudhia A, Funke B, Grabowski U, et al. A blind test retrieval experiment for infrared limb emission spectrometry. J Geophys Res 2003;108(D23): 4746. http://dx.doi.org/10.1029/2003JD003835.
[123] Worden H, Beer R, Rinsland CP. Airborne infrared spectroscopy of 1994 western wildfires. J Geophys Res 1997;102:1287–300, http://dx.doi.org/10.1029/96JD02982.
[124] Dozier J. A method for satellite identification of surface temperature fields of subpixel resolution. Remote Sens Environ 1981;11: 221–9. http://dx.doi.org/10.1016/0034-4257(81)90021-3.
[125] Evans KF, Walter SJ, Heymsfield AJ, Deeter MN. Modeling of submillimeter passive remote sensing of cirrus clouds. J Appl Meteorol 1998;37:184–205. http://dx.doi.org/10.1175/1520-0450 (1998)037(0184:MOSPRS)2.0.CO;2.
[126] Hoepfner M, Emde C. Comparison of single and multiple scattering approaches for the simulation of limb-emission observations in the mid-IR. J Quant Spectrosc Radiat Transfer 2005;91(3): 275–85. http://dx.doi.org/10.1016/j.jqsrt.2004.05.066.
[127] Wu DL, Austin RT, Deng M, Durden SL, Heymsfield AJ, Jiang JH, et al. Comparisons of global cloud ice from MLS, CloudSat, and correlative data sets. J Geophys Res 2009;114:D00A24. http://dx.doi.org/10.1029/2008JD009946.
[128] Rydberg B, Eriksson P, Buehler SA, Murtagh DP. Non-gaussian Bayesian retrieval of tropical upper tropospheric cloud ice and water vapour from Odin-SMR measurements. Atmos Meas Tech 2009;2:621–37. http://dx.doi.org/10.5194/amt-2-621-200.
[129] Millàn L, Read W, Kasai Y, Lambert A, Livesey N, Mendrok J, et al. SMILES ice cloud products. J Geophys Res 2013;118(12): 6468–77. http://dx.doi.org/10.1002/jgrd.50322.
[130] Spang R, Arndt K, Dudhia A, Höpfner M, Hoffmann L, Hurley J, et al. Fast cloud parameter retrievals of MIPAS/Envisat. Atmos Chem Phys 2012;12(15):7135–64. http://dx.doi.org/10.5194/acp-12-7135-2012.
[131] Buehler SA, Defer E, Evans F, Eliasson S, Mendrok J, Eriksson P, et al. Observing ice clouds in the submillimeter spectral range: the CloudIce mission proposal for ESA's Earth Explorer 8. Atmos Meas Tech 2012;5:1529–49. http://dx.doi.org/10.5194/amt-5-1529-2012.
[132] Ekström M, Eriksson P, Rydberg B, Murtagh DP. First Odin sub-mm retrievals in the tropical upper troposphere: humidity and cloud ice signals. Atmos Chem Phys 2007;7:459–69. http://dx.doi.org/10.5194/acp-7-459-2007.
[133] Mendrok J. The SARTre model for radiative transfer in spherical atmospheres and its application to the derivation of cirrus cloud properties [PhD thesis]. Berlin: Freie Universität; June 2006.
[134] Stamnes K, Tsay S-Chee, Wiscombe W, Jayaweera K. Numerically stable algorithm for discrete-ordinate-method radiative transfer in multiple scattering and emitting layered media. Appl Opt 1988;27: 2502–9. http://dx.doi.org/10.1364/AO.27.002502.
[135] Mendrok J, Schreier F, Höpfner M. Estimating cirrus cloud properties from MIPAS data. Geophys Res Lett 2007;34: L08807. http://dx.doi.org/10.1029/2006GL028246.
[136] Rauer H, Gebauer S, von Paris P, Cabrera J, Godolt M, Grenfell JL, et al. Potential biosignatures in super-Earth atmospheres—I. Spectral appearance of super-Earths around M dwarfs. A&A 2011;529:A8. http://dx.doi.org/10.1051/0004-6361/201014368.
[137] Grenfell JL, Grießmeier J-M, von Paris P, Patzer ABC, Lammer H, Stracke B, et al. Response of atmospheric biomarkers to NO_x-induced photochemistry generated by stellar cosmic rays for Earth-like planets in the habitable zone of M dwarf stars. Astrobiology 2012;12(12):1109–22. http://dx.doi.org/10.1089/ast.2011.0682.
[138] Vasquez M, Schreier F, Gimeno García S, Kitzmann D, Patzer B, Rauer H, et al. Infrared radiative transfer in atmospheres of Earth-like planets around F, G, K, and M stars. II Thermal emission spectra influenced by clouds. A&A 2013;557:A46. http://dx.doi.org/10.1051/0004-6361/201220566.
[139] Hedelt P, von Paris P, Godolt M, Gebauer S, Grenfell JL, Rauer H, et al. Spectral features of Earth-like planets and their detectability at different orbital distances around F, G, and K-type stars. A&A 2013;553:A9. http://dx.doi.org/10.1051/0004-6361/201117723.
[140] Hedelt P, Alonso R, Brown T, Collados Vera M, Rauer H, Schleicher H, et al. Venus transit 2004: illustrating the capability of exoplanet transmission spectroscopy. A&A 2011;533:A136, http://dx.doi.org/10.1051/0004-6361/201016237.
[141] Gottwald Manfred, Bovensmann Heinrich, editors. SCIAMACHY—exploring the changing Earth's atmosphere. Dordrecht, NL: Springer; 2011 http://dx.doi.org/10.1007/978-90-481-9896-2.
[142] Ngo NH, Lisak D, Tran H, Hartmann J-M. An isolated line-shape model to go beyond the Voigt profile in spectroscopic databases and radiative transfer codes. J Quant Spectrosc Radiat Transfer 2013;129:89–100 ⟨http://dx.doi.org/10.1016/j.jqsrt.2013.05.034⟩.

[143] Boone CD, Walker KA, Bernath PF. Speed-dependent Voigt term profile for water vapor in infrared remote sensing applications. J Quant Spectrosc Radiat Transfer 2007;105: 525–32. http://dx.doi.org/10.1016/j.jqsrt.2006.11.015.
[144] Hartmann J-M, Tran H, Toon GC. Influence of line mixing on the retrievals of atmospheric CO_2 from spectra in the 1.6 and 2.1 μm regions. Atmos Chem Phys 2009;9:7303–12. http://dx.doi.org/10.5194/acp-9-7303-2009.
[145] Schneider M, Hase F, Blavier J-F, Toon GC, Leblanc T. An empirical study on the importance of a speed-dependent Voigt line shape model for tropospheric water vapor profile remote sensing. J Quant Spectrosc Radiat Transfer 2011;112(3):465–74. http://dx.doi.org/10.1016/j.jqsrt.2010.09.008.
[146] Davis PhJ, Rabinowitz Ph. Methods of numerical integration. 2nd ed.New York: Academic Press; 1984.
[147] SLATEC, Common Mathematical Library (Version 4.1). Available from NetLib, ⟨http://www.netlib.org/slatec⟩; July 1993.